Journal of Materials Chemistry A

Accepted Manuscript

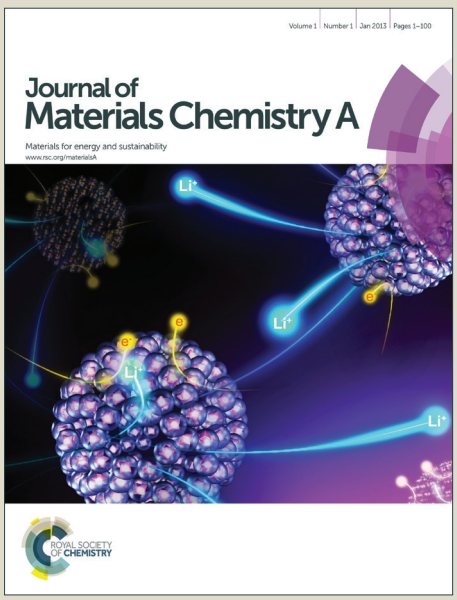

ROYAL SOCIETY OF CHEMISTRY

www.rsc.org/materialsA

Nanostructured robust cobalt metal alloy based anode electro-catalysts exhibiting remarkably high performance and durability for proton exchange membrane fuel cells

Prasad Prakash Patel[1], Moni Kanchan Datta[2,3], Oleg Velikhokhatnyi[2,3], Prashanth Jampani[2], Daeho Hong[2], James A. Poston[4], Ayyakkannu Manivannan[4], Prashant N. Kumta[1,2,3,5,6]

[1]Department of Chemical and Petroleum Engineering, Swanson School of Engineering, University of Pittsburgh, Pittsburgh, PA 15261, USA.

[2]Department of Bioengineering, Swanson School of Engineering, University of Pittsburgh, Pittsburgh, PA 15261, USA.

[3]Center for Complex Engineered Multifunctional Materials, University of Pittsburgh, PA 15261, USA.

[4]US Department of Energy, National Energy Technology Laboratory, Morgantown, WV 26507.

[5]Mechanical Engineering and Materials Science, Swanson School of Engineering, University of Pittsburgh, Pittsburgh, PA 15261, USA.

[6]School of Dental Medicine, University of Pittsburgh, PA 15217, USA.

This is an abstract presented at the 225th Electrochemical Society Meeting in Orlando, FL (May 11-15, 2014).

Abstract

In recent years, the development of durable and electrochemically active electro-catalyst alloys with reduced noble metal content exhibiting similar or better electrochemical performance than pure noble metal catalysts has gathered considerable momentum particularly, for proton exchange membrane fuel cells (PEMFC) application. Engineering such reduced noble metal containing electro-catalyst alloys in the nano-scale dimensions with high active electrochemical surface area (ECSA) will ultimately translate to reduced noble metal loadings to ultra-low levels which will eventually constitute to an overall reduction in the capital cost of PEMFCs. Herein we report the development of nanostructured Co-Ir based solid-solution electro-catalyst alloy for hydrogen oxidation reaction (HOR) further validated by first principles theoretical calculation of the d band center of the transition metal. The theoretical and experimental studies reported herein demonstrate that the nanostructured alloy catalyst comprising 70at.% Co ($Co_{0.7}Ir_{0.3}$) and 60 at.% Co ($Co_{0.6}Ir_{0.4}$) of crystallite size ~4nm with a high electrochemically active surface area (ECSA) (~56 m^2/g) exhibit improved electrochemical activity (reduction in overpotential and improved reaction kinetics) for HOR combined with outstanding durability contrasted with pure Ir nanoparticles (Ir-NPs) as well as state of the art commercial Pt/C system. Moreover, an optimized alloy containing 60 at% Co ($Co_{0.6}Ir_{0.4}$) showed a remarkable ~156% and 92% higher catalytic activity for HOR than Ir-NPs and commercial 40% Pt/C, respectively, with similar loadings and ECSA. The single PEMFC full cell study shows ~85% improved maximum power density for $Co_{0.6}(Ir_{0.4})$ catalyst compared to 40% Pt/C and excellent electrochemical stability/durability comparable to 40% Pt/C.

Keywords

PEM fuel cell; electro-catalyst; hydrogen oxidation reaction; iridium; cobalt; nanostructured metal alloys; solid solution

1. Introduction

The growing environmental concerns due to rapid depletion of fossil fuels necessitates a need for the efficient use of energy, and more importantly, exploration of renewable and clean energy sources.[1-3] In this regard, fuel cell technology has gained considerable attention over the years as it offers one of the promising and sustainable approaches for the continuous production of power with reduced greenhouse gas emissions, and higher efficiency compared to current combustion based technologies. Hence, they are considered to be an ideal energy source for stationary and mobile applications such as automobile, portable devices and materials handling equipment etc.[4, 5]. In particular, proton exchange membrane fuel cells (PEMFCs) have received significant attention as power sources due to the systemic advantages of the use of hydrogen, a light-weight, clean fuel (low carbon footprint) and low operating temperatures (<120^{o}C). Other attributes include quick start-up, extended durability of system components and low weight and volume due to elimination of additional steps of fuel reformation. The simple system design would be reflected in the ease of operation, reduced cost and high reliability.[3, 6-11] Despite these known attributes, the prohibitive capital cost and inferior durability of the system puts severe constraints thus limiting the commercialization of PEMFCs. The typically used expensive platinum group metals (PGM) based electro-catalysts (e.g. Pt/C) possess excellent electrochemical activity and electrochemical stability/durability as PEMFC anode and cathode materials although posing a major economic barrier to large-scale commercialization of

PEMFC.[12-18] Hence, there has been a widespread intense research activity directed at identifying non-noble metal or reduced noble metal containing electro-catalysts exhibiting high electrochemical activity and stability/durability that will minimize precious metal loadings to ultra-low levels. To this extent, several approaches have been explored thus far and there still remains considerable opportunity to not only identify such systems but also develop novel approaches to generate these systems with the required materials and electrochemical attributes.

While identifying systems completely devoid of noble metals is certainly the ultimate goal, there is also a need to develop systems with considerable reduction in noble metal content while not limiting the electrochemical performance. One approach to reduce the noble metal content in anode electro-catalysts is alloying of noble metal (e.g. Pt) with transition metals such as Fe, Sn, Ni, Mo [19-25] without compromising the electrochemical performance. It is known that the high performance of the Pt based metal alloy catalyst is attributed to the decrease in the Pt-Pt interatomic distance, maintenance of good dispersion of Pt over the support and modification of the electronic structure of Pt due to a shift in d-band center, which is responsible for achieving the high catalytic activity due to reduction in adsorption/dissociation energies for hydrogen.[24-26] In addition, it has been suggested that the presence of noble-metal catalysts in conjunction with non-noble materials would result in the formation of micro-electrochemical cells, thus lowering the reaction barrier while at the same time, enhancing the reaction kinetics.[27, 28] Platinum based alloys have also shown good electrochemical performance for fuel cells based on the electro-oxidation of different fuels, such as Pt-Sn/C and Pt-Sn-Ir/C ternary alloy for ethanol oxidation, Pt-Ru, Pt-Ru-Os, Pt-Ru-Os-Ir, Pt-Co, Pt-Ti/C, Pt-Ni-Cr/C and Pt-CuO/C for methanol oxidation, Pt-Ti/C for oxygen reduction reaction (ORR), Pt-Ni/C and Pt-WO_3-TiO_2/C for hydrogen oxidation reaction (HOR) for PEMFC.[19, 24, 29-37] Thus, the alloying approach has been known to

offer reduced noble metal loading without compromising electrochemical performance and stability/durability.

In addition to Pt, Ir and IrO_2 have also been identified as novel electro-catalysts for different electrochemical processes such as ethanol fuel cell, oxygen reduction reaction (ORR) and oxygen evolution reaction in water electrolysis. For example, Ir based catalysts (*e.g.* IrSe/C, Ir-Sn) have shown good electrochemical performance with superior methanol tolerance for direct ethanol fuel cells.[38] Furthermore, alloys based on Co and Ir have shown promising electrochemical activity for ORR.[39-41] Pd-Ir catalysts for direct formic acid fuel cells and IrO_2/Ti and Ir-M-O_x (M=Ru, Mo, W, V) binary/ternary oxide catalysts for ORR and OER including solid solution oxide electro-catalysts with and without F doping, $Ir_{1-x}M_xO_{2-y}F_y$ (M = Sn, Nb,) [42-48] are examples of noble metal catalysts involving Ir-IrO_2 system. Ir/IrO_2 is known to exhibit lower cost than Pt.[17, 18, 39, 40, 49-52] However, there are limited studies on Ir and IrO_2 based catalysts for anode as HOR of PEMFC.[49] Hence, in this study, effort has been made to identify new catalyst systems with much reduction in Ir content as possible HOR anode catalysts. In this study therefore, first-principles calculations of the total energies, electronic structures and cohesive energies of different model systems have been carried out to identify a suitable Co based alloy systems containing Ir for HOR. Based on the theoretical calculations, Co alloys, specifically Co-Ir solid solutions denoted as $Co_{1-x}(Ir_x)$ alloy of different compositions (x=0, 0.2, 0.3, 0.4, 1), as shown in **Fig. 1** corresponding to the Co-Ir binary equilibrium phase diagram, have been explored as an anode electro-catalyst for HOR of PEMFC. It should be noted that solid solutions of $x > 0.4$ have intentionally not been explored since the aim of the study is to use low-noble metal containing alloy systems and compositions rich in Ir content would therefore be superfluous.

In addition to the formation of Co-Ir solid solution, the synthesis of nanostructured Co-Ir alloy with high electrochemical active surface area (ECSA) is equally of paramount importance to improve the reaction kinetics and thus, minimize the electro-catalyst loading. Hence, identification of a synthesis method to form robust and efficient Co-Ir based electro-catalysts with high ECSA is highly desirable and correspondingly, also represents a major challenge in the current experimental research on fuel cells.[13] Reduction of metal precursors by ethylene glycol via commonly known polyol process is a popular synthesis method for Ir-M alloys.[40] However, the addition of HCl in the final step typically results in the dissolution of the transition metal (M). To retain transition metal (cobalt) in the final material in this study, a completely alloyed Co(Ir) alloy in the nanostructured form has been synthesized by a two-step synthesis approach. Co nanoparticles (Co-NPs) are synthesized in the first step by reduction of the cobalt salt precursors, followed by reduction of the iridium precursor to form iridium nanoparticles (Ir-NPs) in the second step on the surface of the Co-NPs to form a composite alloyed NPs. At both stages, $NaBH_4$ is used as a reducing agent with the addition of polyvinylpyrrolidone (PVP) as a surfactant to avoid aggregation of the synthesized particles. The final obtained powder is then heat treated to a moderately low temperature of 200^{o}C in (Ar+6.5% H_2) atmosphere in order to ensure proper alloying of the constituent metals combined with reduction of any unreacted precursor and pyrolysis of any unwanted residue. The present report thus documents the theoretical, physical characterization, and electrochemical performance studies conducted on the nanostructured solid solution of Co and Ir as binary electro-catalysts for HOR of PEMFC.

2. Computational methodology

The overall catalytic activity as well as the long term stability of the Co based $Co_{1-x}(Ir_x)$ solid solution electro-catalysts is expected to depend on the electronic structure. The effect of compositions on the electronic structure and the electrocatalytic activity of the alloy could be best understood from theoretical considerations. The aim of the computational component of the present study is thus to investigate the electronic properties of $Co_{1-x}(Ir_x)$ catalyst as a function of its chemical composition. The total energy, electronic and optimized crystal structures as well as total and projected densities of the electronic states for pure Ir metal and the different $Co_{1-x}(Ir_x)$ solid solutions have been calculated using First Principles approaches within the density functional theory. For comparative purpose, pure platinum which is universally regarded as the gold standard electro-catalyst for PEMFCs has also been considered in the present study.

The HOR as is well-known in PEMFC occurs on the surface of the catalyst and hence there is a need to investigate the electronic and structural properties of the surface of the alloy materials. For these studies, hence the (111) surface has been considered as the most stable crystallographic orientation of the face centered cubic structure for pure Pt and Ir, as well as for Co-Ir solid solutions. Further, for computational simplicity, the following solid solution compositions of Co-Ir have been chosen: $Co_{0.5}(Ir_{0.5})$, $Co_{0.625}(Ir_{0.375})$ and $Co_{0.75}(Ir_{0.25})$. These compositions effectively include the most interesting range of Ir concentrations with substantial reduction in Ir content in the Co-Ir alloys, while also allowing for the selection of a relatively small number of super-cells representative of the reduced Ir containing compositions suitable for the calculation of the surface electronic structures employed in the present study. Thus, for calculation of the (111) surface electronic properties of the solid solution, a two-dimensional slab comprising of a thickness of four atomic layers separated from its image perpendicular to the surface direction by a vacuum layer of ~15 Å has been accordingly selected.

For calculating the total energies, electronic structure and density of electronic states, the Vienna Ab-initio Simulation Package (VASP) was used within the projector-augmented wave (PAW) method [53-55] and the generalized gradient approximation [56] for the exchange-correlation energy functional in a form suggested by Perdew and Wang [57]. This program calculates the electronic structure and the inter-atomic forces determined from First Principles *via* the Hellmann-Feynman theorem. Standard PAW potentials were employed for the Ir, Co and Pt potentials containing nine, nine, and ten valence electrons, respectively.

For all alloy compositions considered, the plane wave cutoff energy of 520 eV has been chosen to maintain high accuracy of the total energy calculations. The lattice parameters and internal positions of atoms were fully optimized employing the double relaxation procedure and consequently, the minima of the total energies with respect to the lattice parameters and internal ionic positions have been determined. This geometry for optimization was obtained by minimizing the Hellman–Feynman forces via a conjugate gradient method, so that the net forces applied on every ion in the lattice are close to zero. The total electronic energies were converged within 10^{-5} eV/un.cell resulting in the residual force components on each atom to be lower than 0.01 eV/Å/atom. This will allow an accurate determination of the internal structural parameters corresponding to the alloy. The Monkhorst-Pack scheme was used to sample the Brillouin Zone (BZ) and generate the actual ***k***-point grid for all the alloy compositions considered in the present study. A choice of the appropriate number of ***k***-points in the irreducible part of the BZ was based on convergence of the total energy to 0.1 meV/atom.

3. Experimental Methodology

3.1 Synthesis of $Co_{1-x}(Ir_x)$ electro-catalyst

Synthesis of Ir-NPs (x=1 of $Co_{1-x}Ir_x$)

Ir-NPs were synthesized by the reduction of hydrogen hexachloroiridate (IV) hydrate ($H_2IrCl_6.xH_2O$, 99.98%, Aldrich) using sodium borohydride ($NaBH_4$, 12 wt. % in 14 M NaOH, Aldrich) as the reducing agent.[58] $H_2IrCl_6.xH_2O$ was dissolved in ethanol (≥99.5%, Aldrich) to which polyvinylpyrrolidone (PVP, Alfa Aesar) was added as a surfactant under stirring. The solution was then adjusted to pH 12 by the addition of NaOH/ethanol solution followed by heating to 65 ± 5^0C. After 1 h stirring at 65 ± 5^0C, excess $NaBH_4$ solution was added drop wise under vigorous stirring into the $H_2IrCl_6.xH_2O$ solution to form the Ir-NPs by precipitation. The temperature was maintained at 65 ± 5^0C for 1 h. To avoid any deleterious side-reaction with air, the reduction of $H_2IrCl_6.xH_2O$ was carried out in high purity N_2 (Matheson; 99.99%, flow rate = 100cm^3/min) atmosphere. The resultant Ir-NPs were centrifuged and washed repeatedly with water purified by the Milli-Q system (18 MΩ cm deionized water, Milli-Q Academic, Millipore) and ethanol followed by drying at 50^0C for 6 h. To eliminate any unwanted residue (e.g. PVP), and ensure the complete reduction of any unreacted $H_2IrCl_6.xH_2O$ as well, the final Ir-NPs were heat-treated at 200^0C in a tube furnace utilizing a mixture of Ar and 6.5% H_2 gas (Matheson; 99.99%, flow rate = 100cm^3/min) for 2 h.[59]

Synthesis of Co-NPs (x=0 of $Co_{1-x}Ir_x$)

Co-NPs were also synthesized by chemical reduction of cobalt chloride hexahydrate ($CoCl_2.6H_2O$, 98%, Aldrich) using sodium borohydride ($NaBH_4$, 12 wt. % in 14 M NaOH, Aldrich) as the reducing agent.[58] $CoCl_2.6H_2O$ was dissolved in ethanol (≥99.5%, Aldrich) along with polyvinylpyrrolidone (PVP, Alfa Aesar) and then subsequently reduced using $NaBH_4$ solution to form Co-NPs in a procedure similar to that used to obtain Ir-NPs as explained above.

A similar heat-treatment methodology, that was used in the synthesis of Ir-NPs, was employed to obtain residue-free Co-NPs.[59]

Synthesis of $Co_{1-x}(Ir_x)$ (x = 0.2, 0.3, 0.4)

Solid solution of $Co_{1-x}(Ir_x)$ was synthesized by the reduction of hydrogen hexachloroiridate (IV) hydrate ($H_2IrCl_6.xH_2O$, 99.98%, Aldrich) using $NaBH_4$ in the presence of as-synthesized Co-NPs followed by thermal treatment at 200^0C under Ar+6.5% H_2 mixture. In this procedure, the as-synthesized Co-NPs were dispersed in ethanol (≥99.5%, Aldrich), to which PVP as surfactant was added under stirring. To this solution subsequently, stoichiometric amount of $H_2IrCl_6.xH_2O$ was added followed by pH adjustment to 12 using NaOH/ethanol solution. The solution was then heated to 65 ± 5^0C. After 1 h stirring at 65 ± 5^0C, excess $NaBH_4$ (12 wt. % in 14 M NaOH, Aldrich) solution was added drop wise under the vigorous stirring into the Co-NPs dispersed solution to form Ir-NPs on the surface of Co-NPs, resulting in the formation of solid solution of $Co_{1-x}(Ir_x)$. The temperature was maintained at 65 ± 5^0C for 1 h. To avoid the oxidation of Co nanoparticles, high purity N_2 (Matheson; 99.99%, flow rate = 100 cm^3/min) was kept flowing during the entire synthesis procedure. The resultant electro-catalyst was centrifuged and washed repeatedly with water purified by the Milli-Q system (18 MΩ cm deionized water, Milli-Q Academic, Millipore) and then ethanol, followed by drying at 50^0C for 6 h. To ensure complete reaction between Co and Ir and formation of a homogeneous solid solution of $Co_{1-x}(Ir_x)$ as well as remove any unwanted residue from the final product, the final $Co_{1-x}(Ir_x)$ powder was heat-treated at 200^0C in a tube furnace using a mixture of Ar and 6.5% H_2 gas (Matheson; 99.99%, flow rate = 100 cm^3/min) for 2 h.[59]

3.2 Electro-catalyst Characterization

3.2.1 Structural characterization

X-ray diffraction

X-ray diffraction (XRD) using Philips XPERT PRO system employing CuK_{α} ($\lambda = 0.15406$ nm) radiation at an operating voltage and current of 45 kV and 40 mA was utilized to perform qualitative and quantitative phase analysis of the synthesized $Co_{1-x}(Ir_x)$ solid solution electro-catalysts of different compositions. The XRD peak profile of $Co_{1-x}(Ir_x)$ was analyzed using the Pseudo-Voigt function to determine the Lorentzian and Gaussian contribution of the peak. The integral breadth of the Lorentzian contribution, determined from peak profile analysis using the single line approximation method after eliminating the instrumental broadening and lattice strain contribution, was used in the Scherrer formula to calculate the particle size of the $Co_{1-x}(Ir_x)$ solid solution corresponding to different compositions.[60] The lattice parameter and molar volume of the synthesized $Co_{1-x}(Ir_x)$ alloy of different compositions have been calculated using the least square refinement techniques.

Microstructure analysis

The microstructure of $Co_{1-x}(Ir_x)$ solid solution electro-catalyst of different compositions was analyzed using scanning electron microscopy (SEM). Accordingly, quantitative elemental analysis and distribution of the respective elements utilizing x-ray mapping was performed exploiting the energy dispersive x-ray spectroscopy (EDAX) analyzer attached to the SEM equipment. Moreover, a Philips XL-30FEG equipped with an EDAX detector system comprised of an ultrathin beryllium window and Si(Li) detector operating at 20 kV was used for performing elemental and x-ray map analysis. Additionally, transmission electron microscopy and high

resolution transmission electron microscopy (HR-TEM) was conducted using the JEOL JEM-2100F to evaluate the particle size and the structure of alloyed $Co_{1-x}(Ir_x)$ particles. The specific surface area (SSA) of the electro-catalyst materials was also determined by conducting nitrogen adsoption-desorption studies and analyzing the data using the Brunauer-Emmett-Teller (BET) isotherms. The powder was first vacuum degassed and then tested using a Micromeritics ASAP 2020 instrument. Multipoint BET specific surface areas have been obatined and reported for the synthesized solid solution electro-catalyst powders.

X-ray photoelectron spectroscopy

X-ray photoelectron spectroscopy (XPS) was performed on the solid solution electro-catalysts to determine the electronic states of Ir and Co in $Co_{1-x}(Ir_x)$ solid solutions. The XPS has been carried out using a Physical Electronics (PHI) model 32-096 X-ray source control and a 22-040 power supply interfaced to a model 04-548 X-ray source with an Omni Focus III spherical capacitance analyzer (SCA). The system is routinely operated within the pressure range of 10^{-8} to 10^{-9} Torr (1.3×10^{-6} to 1.3×10^{-7} Pa). The system was calibrated in accordance with the manufacturer's procedures utilizing the photoemission lines E_b of Cu $2p_{3/2}$ (932.7 eV), E_b of Au $4f_{7/2}$ (84 eV) and E_b of Ag $3d_{5/2}$ (368.3eV) for magnesium anode. All the reported intensities were obtained by dividing the experimentally determined peak areas by the instrumental sensitivity factors. Charge correction was obtained by referencing the adventitious C 1s peak to 284.8 eV.

3.2.2 Electrochemical characterization

Electrochemical characterization was conducted in the presence of H_2 saturated 0.5 M sulfuric acid (H_2SO_4) at 40^0C (using a Fisher Scientific 910 Isotemp refrigerator circulator) in an electrochemical workstation (VersaSTAT 3, Princeton Applied Research) using a three electrode cell configuration, which was initially saturated with ultra-high purity (UHP)-N_2 to expel oxygen in the solution. The working electrodes were prepared by spreading the electro-catalyst ink of $Co_{1-x}(Ir_x)$ (x = 0.2, 0.3, 0.4, 1) on teflonized carbon paper. The ink comprised 85 wt% catalyst and 15 wt% Nafion 117 (5 wt.% solution in lower aliphatic alcohols, Aldrich). The total loading of the $Co_{1-x}(Ir_x)$ electro-catalyst (x = 0.2, 0.3, 0.4, 1) was maintained at ~0.4 mg on 1 cm^2 area irrespective of the composition. In this study, it should be noted that the electrochemical performance of pure Ir-NPs (x=1) and $Co_{1-x}(Ir_x)$ alloy solid solution is compared with the state of the art commercially obtained Pt/C based electro-catalyst. Accordingly, the electrochemical performance of commercially obtained 40% Pt/C electro-catalyst (Alfa Aesar) was studied with loading of ~0.4 mg of Pt on 1 cm^2 area under identical operating conditions. A Pt wire was used as the counter electrode and mercury/mercurous sulfate (Hg/Hg_2SO_4) electrode (XR-200, Hach) that has a potential of +0.65 V with respect to normal hydrogen electrode (NHE) was used as the reference electrode. All the potential values discussed in this study are with respect to NHE.

Cyclic voltammetry

The electrochemical activity of the electro-catalysts for HOR has been determined by conducting cyclic voltammetry (CV) by scanning the potential between -0.092 V and 1 V at scan rate of 10 mV/sec. The current at 0 V (*vs* NHE, the typical standard redox potential of HOR) in iR_Ω corrected (R_Ω, the ohmic resistance was determined from electrochemical impedance spectroscopy analysis described below) anodic part of CV curves of electro-catalysts

was used to compare the electrochemical performance of the different electro-catalyst materials. The electrochemical active surface area (ECSA) is evaluated for all electro-catalyst materials from anodic part of underpotential deposited hydrogen region of CV curves, obtained in N_2 saturated 0.5 M H_2SO_4 solution, by using the following equation:

$$\mathrm{ECSA} = \frac{\mathrm{Q_r}}{\mathrm{mc}}$$

where, 'Q_r' is the integrated area of anodic part of underpotential deposited hydrogen region in the CV curve, 'm' is the loading of the iridium/platinum and '*c*' is the electrical charge associated with monolayer adsorption of hydrogen on Ir (220 μC/cm^2)/ Pt (210 μC/cm^2).[17, 49, 61] A 0.5 M H_2SO_4 solution was initially saturated with N_2 to remove oxygen present in the solution. The Tafel plot after iR_Ω correction given by the equation $\eta = a + b \log i$ (plot of overpotential η *vs* log current, log *i*) and the corresponding Tafel slope (b) has been used to determine the reaction kinetics.

Electrochemical impedance spectroscopy

Electrochemical impedance spectroscopy (EIS) was carried out to determine the ohmic resistance (R_Ω) (which includes the resistance of various components including, electrolyte, and catalyst layer) and charge transfer resistance (R_{ct}) of electro-catalysts. EIS has been conducted in the frequency range of 100 mHz-100 kHz at ~0.016 V (*vs* NHE), which is near to the standard potential used for assessing electro-catalyst activity (0 V) for HOR in H_2 saturated 0.5 M H_2SO_4 solution at 40^{0}C using the electrochemical work station (VersaSTAT 3, Princeton Applied Research). The experimentally obtained EIS plot was fitted using the ZView software from Scribner Associates with a circuit model $R_\Omega(R_{ct}Q_1W_o)$, where Q_1 is the constant phase element (CPE), representing the capacitance behavior of the electro-catalyst surface.[46] R_Ω was used for

316 ohmic correction (iR_Ω) in CV curves and the polarization resistance of synthesized electro-
317 catalysts was evaluated by R_{ct}.[47]
318
319 *Reaction kinetics study*
320 To study kinetics of the HOR reaction, polarization studies were performed using a
321 rotating disk electrode (RDE) setup. The catalyst ink (85 wt% catalyst and 15 wt% Nafion 117)
322 was sonicated and applied to a glassy carbon (GC) disk (geometric area=0.19 cm^2). After solvent
323 evaporation, the GC surface had a thin layer of electro-catalyst, which served as the working
324 electrode. A Pt wire was used as the counter electrode and Hg/Hg_2SO_4 was used as the reference
325 electrode. HOR evaluation was carried out in 0.5 M H_2SO_4 solution at 40^0C in H_2 stream. The
326 total loading of $Co_{1-x}(Ir_x)$ (x=0.2, 0.3, 0.4, 1) was 100 μg cm^{-2} and the total loading of
327 commercial 40% Pt/C (Alfa Aesar) was also 100 μg (of Pt) cm^{-2}. The solution was initially
328 saturated with N_2 to remove oxygen present in the solution. The rotation speed was maintained at
329 100, 400, 900, 1600 and 2500 rpm, respectively. Polarization was conducted in multiple small
330 potential steps (**Fig. S1**) on the RDE to reduce the contribution by the charging current and the
331 current measurement was performed at the end of each step.[62] The Koutechy-Levich equation
332 was used to determine the number of electrons (n) produced in the reaction and the kinetic
333 current (i_k).[62]

334 $$i^{-1} = i_k^{-1} + i_L^{-1}$$

335 $$i_L = 0.620\, n\, F\, A_e\, D_0^{2/3}\, \omega^{1/2}\, \nu^{-1/6}\, C_o^*$$

336 Here, i_L is the limiting current (A, Ampere), i_k is the kinetic current (A, Ampere) observed in the
337 absence of any mass transfer limitation, F is Faraday constant (C/mol), A_e is the geometric area
338 of electrode (0.19 cm^2), D_0 is diffusivity (cm^2/sec), ω is rotation speed (rad/sec), ν is the

kinematic viscosity of the electrolyte and C_o^* is the bulk concentration of H_2 in 0.5 M H_2SO_4 solution.

Electrochemical stability/durability test

To study the electrochemical stability/durability of $Co_{1-x}(Ir_x)$ (x=0.2, 0.3, 0.4, 1) solid solution electro-catalysts, chronoamperometry (CA) (current *vs* time) was performed for 24 h using H_2 saturated 0.5 M H_2SO_4 as the electrolyte solution maintained at 40^0C at the constant voltage of ~0.016 V (*vs* NHE). Elemental analysis of the electrolyte (H_2SO_4), collected after 24 h of CA testing, was performed by inductively coupled plasma optical emission spectroscopy (ICP-OES, iCAP 6500 duo Thermo Fisher) to determine the amount of cobalt and iridium leached out into the electrolyte solution from the electrode providing information about the electrochemical stability of the electro-catalyst.

Membrane electrode assembly (MEA) preparation and single cell test analysis

The anode and cathode catalyst ink was prepared consisting of 85 wt.% catalyst and 15 wt.% Nafion 117 solution (5 wt.% solution in lower aliphatic alcohols, Sigma-Aldrich). For anode, the total loading of $Co_{1-x}(Ir_x)$ (x=0.3, 0.4) electro-catalyst was 0.2 mg/cm^2. For comparison, 40% Pt/C (Alfa Aesar) was also studied as anode electro-catalyst in single cell test using loading of ~0.2 mg of Pt/cm^2. On the other hand, the cathode catalyst ink was prepared using 40% Pt/C electro-catalyst (Alfa Aesar). Loading of 0.3 mg of Pt/cm^2 was used for cathode electro-catalyst. The electrodes were prepared by spreading the electro-catalyst ink on teflonized carbon paper. For the single cell testing, a membrane electrode assembly was fabricated by using a Nafion 115 membrane which was sandwiched between the anode and cathode. The Nafion 115

membrane was pretreated first with 3 wt.% hydrogen peroxide solution to its boiling point to oxidize any organic impurities. Subsequently, it was boiled in D.I. water followed by immersion in boiling 0.5 M sulfuric acid solution to eliminate impurities. Finally, it was washed multiple times in D.I water to remove any traces of remnant acid. This membrane was then stored in D.I. water to avoid dehydration. The sandwiching of Nafion 115 membrane between anode and cathode was carried out by hot-pressing in a 25T hydraulic lamination hot press with dual temperature controller (MTI Corporation) at a temperature of 125^0C and pressure of 40 atm applied for 30 sec to ensure good contact between the electrodes and the membrane. This MEA was then used in the single cell test analysis, carried out for 24 h using fuel cell test set up obtained from Electrochem Incorporation at 80^oC and 0.1 MPa with UHP-H_2 (200 ml/min) and UHP-O_2 (300 ml/min) as reactant gases.

4. Results and discussion

4.1 Comparison of electrochemical performance of Ir-NPs with commercially obtained Pt/C

4.1.1 Structural characterization of Ir-NPs

The XRD pattern of the pure Ir-NPs synthesized by the reduction of $H_2IrCl_6.xH_2O$, displayed in **Fig. 2**, shows a face centered cubic structure (fcc) with a lattice parameter a= 0.3834 nm and a molar volume (V_m) ~8.49 cm^3/mol, which is in good agreement with the literature value.[63] The particle size of the synthesized Ir-NPs, calculated using the Scherrer's formula utilizing the integral breadth of the Lorenzian contribution of the XRD peak, is ~7 nm. A detailed TEM/HRTEM study (**Fig. S2**) confirms the presence of nanometer sized particles

(~6-9 nm) of Ir-NPs with the fcc crystal structure showing lattice fringes with a spacing of ~0.22 nm corresponding to the (111) inter-planer spacing of face centered cubic Ir. The BET surface area of the Ir-NPs, measured by the N_2 multilayer adsorption/desorption isotherm, is ~29 m^2/g, whereas the ECSA, shown in **Fig. S18**, is ~14.5 m^2/g (**Table 1**). On the other hand, the ECSA of the commercially obtained 40% Pt/C electro-catalyst (**Fig. S18**) is ~55.2 m^2/g which is similar to that reported earlier[17, 49, 64, 65] and four-fold higher than the synthesized Ir-NPs (~14.5 m^2/g).

4.1.2 Electrochemical characterization of synthesized Ir-NPs and commercial 40% Pt/C

The synthesized Ir-NPS were studied in detail for their electrochemical characteristics and furthermore to compare their electrochemical performance with commercially obtained Pt/C. The anodic part of CV curve (**Fig. S3**) (between -0.05 V to 0.2 V *vs* NHE) for HOR of Ir-NPs, measured in H_2 saturated 0.5 M H_2SO_4, shown in **Fig. 3** before and after iR_Ω correction, exhibits an onset potential ~(-0.015V) which is ~ 0.01V higher than the onset potential (as a result of over-potential) of commercial Pt/C ~(-0.025V) (**Table 2**). This result clearly suggests that the chemically synthesized Ir-NPs exhibits higher reaction polarization in the tafel step (*i.e.* $H_2 + 2M \rightarrow 2MH_{ad}$, M=electro-catalyst) for HOR than the Pt/C electro-catalyst. It should be noted that iR_Ω correction of Ir-NPs and Pt/C has been performed after measuring the ohmic resistance (R_Ω~14.5 Ωcm^2) from the EIS analysis, which has been discussed in detail in the later sections to follow. The current density of Ir-NPs (~0.54 mA/cm^2) at ~0 V *vs* NHE is correspondingly ~25% lower than that of the commercially obtained Pt/C (~0.71 mA/cm^2), primarily due to the ~0.01 V higher onset potential of Ir-NPs electro-catalyst with respect to Pt/C (**Table 2**). In addition, it has

been determined from the Tafel polarization plots of Ir-NPs and Pt/C (**Fig. S4** and **S5**) that the measured Tafel slope for pure Ir-NPs (~72 mV/dec) is higher than that of Pt/C (~67 mV/dec), which suggests the sluggish reaction kinetics and higher activation polarization during the Volmer step ($MH_{ad} \rightarrow M + H^+ + e^-$) of HOR for Ir-NPs electro-catalyst compared to that of Pt/C. The higher value of charge transfer resistance (R_{ct}) of Ir-NPs (~24 Ωcm^2) (**Table 3**), determined from the EIS analysis which will be discussed in detail later, compared to commercially obtained Pt/C electro-catalyst (~13 Ωcm^2) (**Table 3**) also validates the slower reaction kinetics (higher activation polarization) of the chemically synthesized Ir-NPs, in comparison to commercially obtained Pt/C.

4.2 Computational study to predict the binary alloy compositions exhibiting high electrochemical activity

The above results clearly suggest that the reaction polarization in the Tafel step and activation polarization in the Volmer step as well as reaction kinetics of HOR for the synthesized Ir-NPs electro-catalyst is higher in comparison to Pt based commercial system. In this study, we define the resistance to the oxidation reaction pathway occurring as a result of the non-Faradaic sub-steps such as specific adsorption, desorption and re-orientation steps as in the 'reaction-polarization' (Tafel-like steps).[66] In HOR, the electron transfer occurs via a number of sub-steps and the barrier to such processes is grouped together in this manuscript and referred to as 'activation polarization' (Heyrovsky/Volmer like steps).[66, 67] Similarly, it has been identified that the reaction kinetics, which is related to the rate of adsorption/desorption of reactants (H_2 in the

present study) and products on the catalytic surface, also known as reaction polarization, is slower for the Ir-NPs electro-catalyst compared to Pt/C. The overall polarization of a chemical reaction can indeed be correlated with an optimal position of the d-band center located in the vicinity of the Fermi level. During the last decade, a wide spread concept has been proposed by J.K. Norskov *et.al.* relating to the existence of a simple descriptor for determining the surface catalytic activity of the transition metals and their alloys. [68, 69] This descriptor has been defined as a gravity center of the transition metal d-band ε_d usually located in the vicinity of the Fermi level. An optimal position of the d-band center thus provides a highly favorable interaction between the catalytic surface and the various species participating in the catalytic reactions predominantly occurring on the surface, leading to the optimal catalytic activity with reduced reaction polarization and possibly reduced activation polarization due to improvement in reaction kinetics. Thus, such an interaction could be considered as "just appropriate" leading to a moderate effect allowing the reactants and products to both adsorb at the surface and also desorb most efficiently. Hence, it can be construed that such an adjustment of the d-band center position with respect to the Fermi level may likely play a critical role contributing to the design of novel highly active and electrochemically stable electro-catalysts which is discussed herein.

Fig. 4 shows the projected d-band densities of states together with the corresponding centers of these zones marked with vertical arrows on the graphs for both pure Pt and Ir. In the present study, the electronic structure of the stable (111) surfaces for all the studied transition metals and their alloys have been calculated and the positions of corresponding d-band centers have been obtained as a first moment of $n_d(E)$: $\varepsilon_d = \int n_d(E) E \mathrm{d}E / \int n_d(E) \mathrm{d}E$, where $n_d(E)$ is the projected d-band density of states of the corresponding solid solutions. Since pure Pt is considered as the gold standard for PEMFC electro-catalyst, the d-band position for Pt marked

with a dashed vertical line, could serve as a reference point or a benchmark for achieving the minimum polarization and correspondingly, the optimal catalytic activity for the designed systems. A close match of the corresponding d-band center to that of the pure Pt d-band center position could imply correspondingly, an improved overall catalytic activity of the studied system due to the expected lower catalytic reaction over-potential. Thus, from **Fig. 4**, it can be identified that the d-band center of pure Ir is located lower on the energy scale than the ideal position corresponding to that of pure Pt and therefore, it is indeed expected to demonstrate higher polarization and a higher over-potential thus leading to a lower catalytic activity compared to pure Pt, which is in good agreement with the obtained experimental results herein.

In order to therefore minimize the electrochemical activation polarization, reaction polarization and thus, the overall over-potential, and correspondingly, improve the reaction kinetics of Ir based electro-catalyst, the Co-based binary Co-Ir system has been explored as a suitable electro-catalyst for HOR in this study. The calculated d band center of the Co based Co-Ir solid solution denoted as $Co_{1-x}(Ir_x)$ of different compositions is also plotted in **Fig. 4**. Generating a solid solution of Ir with 50 at% of Co (x=0.5) shifts the resulting d-band center up closer to the Pt benchmark line, thus minimizing the polarization and enhancing the overall catalytic activity. Such an upward shift is due to the introduction of Co 3d-band located higher in energy than corresponding Ir 5d-band. Further increase of Co content results in a gradual movement of the overall Ir5d-Co3d-band center upward on the energy scale. Thus, according to the corresponding ε_d positions for the calculated Co-Ir alloy solid solutions, a minimum polarization and maximum catalytic activity might be expected for the compound containing ~60at.% Co-40at.% Ir since as shown in **Fig. 4**, for the composition containing 62.5 at % of Co, the ε_d is just below the benchmark line displayed in **Fig. 4**. The last considered alloy with

474 75 at.% of Co (x=0.25) is expected to demonstrate qualitatively similar electro-catalytic
475 performance as pure Ir since the corresponding d-band centers for the two systems are located at
476 almost the same distance around the Pt benchmark line.

477 It should be noted however that the d-band center concept is only a *qualitative* descriptor
478 of the surface reactivity and does not provide an absolute measure of the catalytic activity. It
479 only points to the fact that due to an appropriate change in the electronic structure (in particular,
480 the electronic d-bands) during alloying of Ir with Co, the interatomic interactions between the
481 catalytic surface and different intermediate species involved in the hydrogen oxidation process
482 become most optimal for Co-40at% Ir solid solution and hence the catalytic activity of this alloy
483 is expected to be the highest compared to other chemical compositions in the Co-Ir system
484 demonstrating the potential of using Co modified by the introduction of Ir and hence stabilizing
485 the fcc phase of Co. However, although serving as a descriptor, such a qualitative approach does
486 not provide an accurate explanation and an exact reason for the Co alloys containing 40 at% of Ir
487 predictably demonstrating better electrochemical performance compared to pure Pt. Detailed
488 atomistic consideration of all the elementary reaction steps occurring at the surface of the
489 nanostructured alloy electro-catalysts during HOR could shed further light on the origin of this
490 remarkably noticeable difference between the electro-catalytic activities of experimentally
491 studied compositions of $Co_{0.6}(Ir_{0.4})$, $Co_{0.7}(Ir_{0.3})$ alloys (discussed later) and Pt/C. Such a
492 comprehensive study though not the focus of the present work is clearly warranted and will be a
493 subject of future computational and experimental research. Nevertheless, based on the predicted
494 response determined by the d-band center calculations described above, Co-Ir alloys of different
495 compositions were synthesized and characterized for their electrochemical response as described
496 in the sections to follow.

4.3 Synthesis and characterization of theoretically predicted Co-Ir alloy compositions

4.3.1 Structural characterization of $Co_{1-x}(Ir_x)$

X-ray diffraction study

Nanocrystalline $Co_{1-x}(Ir_x)$ solid solution corresponding to different compositions (x=0, 0.2, 0.3, 0.4, 1) as shown in **Fig. 1** have been accordingly synthesized in order to experimentally verify the theoretical predicted results.[70] The XRD patterns of the chemically synthesized $Co_{1-x}(Ir_x)$ (x = 0, 0.2, 0.3, 0.4, 1) solid solutions are shown in **Fig. 2**. The XRD pattern of pure Co (x=0) shows the expected hcp structure of lattice parameters, *a*= 0.2505 nm, *c*=0.4071 nm with a molar volume ~6.66 cm^3/mol, which is in good agreement with the reported literature value.[71] On the other hand, prevalence of a single phase crystalline fcc solid solution structure is observed for $Co_{1-x}(Ir_x)$ of x=0.3 and 0.4, whereas a two–phase mixture of fcc and hcp crystal structure is detected for $Co_{1-x}(Ir_x)$ (x=0.2) (**Fig. 2**). The variation of molar volume of fcc-$Co_{1-x}(Ir_x)$ with Ir content, shown in **Fig. 5a** and **Table 1**, shows a linear increase in molar volume with Ir content following the Vegard's law suggesting the formation of a solid solution of Ir and Co with fcc structure. This linear rise in molar volume of $Co_{1-x}(Ir_x)$ following increase in Ir content can be explained as occurring due to the higher atomic radius of Ir (~180 pm) compared to Co (~152 pm).[71] It must also be mentioned here that the synthesized $Co_{1-x}(Ir_x)$ solid solution is stable exhibiting the fcc crystal structure in contrast to the expected thermodynamically stable equilibrium hcp phase, as evidenced in the Co-Ir binary alloy phase diagram (**Fig. 1**). This preponderant stability of the fcc structure over the hcp structure can be explained by the allotropic transformation occurring during the refinement of the particle size below a critical

519 value, which is mainly governed by the significant contribution of interfacial/surface energy on
520 the total free energy of the nanocrystalline material.[72, 73]

521 The variation in particle size of $Co_{1-x}(Ir_x)$, calculated using the Scherrer's formula
522 following the XRD peak broadening analysis, also shown in **Fig. 5a** and **Table 1**, indicates a
523 drastic decrease in particle size by the introduction of Ir into the Co lattice, which may be due to
524 lattice softening and solute solution pinning limiting the grain growth of the solid solution.[73, 74]
525 The particle size of $Co_{1-x}(Ir_x)$, with x=0.3 and 0.4, is ~4 nm, which is expected to be below the
526 critical particle size, wherein the fcc cobalt is known to be stable over the normal equilibrium
527 hcp structure due to significant contribution of the interfacial energy thus validating the observed
528 experimental result.[72, 73]

529

530

531

532 *TEM/HR-TEM study*

533 The TEM bright field image along with particle size distribution of $Co_{0.6}(Ir_{0.4})$, displayed
534 in **Fig. 5b**, shows nanometer sized particles of the solid solution in the size range ~4-7 nm which
535 is in good agreement with the XRD analysis. The HRTEM image of $Co_{0.6}(Ir_{0.4})$, shown in **Fig.**
536 **5c**, shows lattice fringes with a spacing of ~0.215 nm which corresponds well with the (111)
537 inter-planer spacing of fcc Co(Ir) determined from XRD analysis. Similarly, the TEM/HRTEM
538 images of $Co_{0.7}(Ir_{0.3})$, shown in **Fig. S6**, also confirms the formation of nanometer sized Co(Ir)
539 particles in the ~5-9 nm range with a lattice spacing of ~0.213 nm also corresponding to the
540 (111) inter-planar spacing of the fcc Co(Ir) alloy.

541

BET/ECSA surface area measurement

The measured BET surface area and ECSA of $Co_{1-x}(Ir_x)$ are given in **Table 1** and plotted in **Fig. 5d**. As shown in **Fig. 5d**, the BET surface area and ECSA follow a similar trend with the variation in particle size *vs* iridium content (**Fig. 5a**), as expected. The ECSA of $Co_{1-x}(Ir_x)$ with x=0.3, 0.4 (~55-56 m^2/g) is almost three-four fold higher than that of pure Ir and $Co_{0.8}(Ir_{0.2})$ (~14-19 m^2/g). This result clearly suggests that $Co_{1-x}(Ir_x)$ with x=0.3 and 0.4 alloys likely possess more number of catalytically active sites than $Co_{0.8}(Ir_{0.2})$ and pure Ir due to the higher ECSA. It must also be mentioned here that the ECSA of commercial Pt/C electro-catalyst (~55.2 m^2/g) is also in the same range of the Co-Ir alloys with x=0.3 and 0.4 (**Table 1**). This result clearly suggest that the two step synthesis strategy implemented herein involving the reduction of the Co and Ir precursors by sodium borohydride and PVP as stabilizer for the synthesis of binary Co-Ir solid solution is indeed a novel approach to generate high ECSA without the addition of high surface area supports (e.g. Vulcan Carbon) that is traditionally employed in currently used hitherto noble metal catalysts including Pt.

SEM/EDAX study

The SEM image along with EDAX pattern of a representative composition $Co_{0.6}(Ir_{0.4})$, collected in **Fig. 6**, shows the presence of Co and Ir. Quantitative elemental composition analysis of the $Co_{1-x}(Ir_x)$ electro-catalyst of different compositions obtained by EDAX confirmed that the measured elemental compositions of Co and Ir are in close agreement to the nominal composition (**Table 1**). Chlorine and carbon peaks could not be detected in the EDAX spectra of all compositions, which indicate that complete removal of chloride ions and carbon (*viz.* stabilizer) has been achieved in the final powder. The elemental x-ray mapping of Co and Ir of

$Co_{0.6}(Ir_{0.4})$ (**Fig. 6**) confirms that Co and Ir are homogeneously distributed within the particles. The SEM image along with EDAX and x-ray mapping of other compositions (x= 0.2, 0.3 and 1) are shown in the supporting information (**Figs. S7-S9**).

X-ray photoelectron spectroscopy study

X-ray photoelectron spectroscopy (XPS) was conducted on the $Co_{1-x}(Ir_x)$ electro-catalyst to determine the surface composition and the chemical oxidation states of Co and Ir in the alloyed compositions. The XPS spectra of Ir and Co of $Co_{1-x}(Ir_x)$ (x = 0.2, 0.3, 0.4, 1) are shown in **Fig. 7 (a-b)**, respectively. The XPS spectrum for pure Ir shows the presence of Ir $4f_{5/2}$ and $4f_{7/2}$ peaks corresponding to the zero oxidation state of Ir centered at ~63.8 eV and ~60.8 eV, which is consistent with the values observed in bulk Ir.[75] For $Co_{1-x}(Ir_x)$ (x=0.2, 0.3 and 0.4), a shift in the Ir $4f_{5/2}$ peak maxima by ~0.33 eV, ~0.24 eV and ~0.22 eV to lower binding energy is observed, which suggests a modification in the electronic structure of Ir.[76, 77] Similarly, the peak maxima of Ir $4f_{7/2}$ peak is also shifted by ~0.28 eV, ~0.24 eV and ~0.07 eV to lower binding energy for $Co_{1-x}(Ir_x)$ (x=0.2, 0.3 and 0.4), respectively, which also indicates a modification in the electronic structure of Ir in the alloyed structure referring to the ability of electron transitions to occur in Ir in the alloyed structure.[78-80] Additionally, the XPS spectrum of pure Co portrayed in **Fig. 7b**, shows the presence of Co $2p_{1/2}$ and $2p_{3/2}$ peaks at ~793.25 eV and ~777.74 eV, corresponding to the zero oxidation state of Co. In the case of $Co_{1-x}(Ir_x)$ (x=0.2), the Co maxima are shifted by ~0.05 eV and ~0.06 eV to slightly lower binding energy than that of pure Co, [81] again suggesting a modification of the electronic structure of cobalt referring to the possible ease of electron transitions occurring in these systems. Similarly, shift in the Co $2p_{1/2}$ peak by ~0.1 eV and ~0.2 eV to lower binding energy is observed for $Co_{1-x}(Ir_x)$ (x=0.3 and 0.4), respectively. The

maxima of Co $2p_{3/2}$ peak is also shifted to slightly lower binding energy by ~0.15eV and ~0.2eV for $Co_{1-x}(Ir_x)$ (x=0.3 and 0.4), respectively, which suggests modification in electronic structure of Co and the possible ease of electronic transitions in these newly formed alloys. [76, 77] Furthermore, the surface atomic ratio of Ir/Co and composition, determined by XPS, is 1.57 (39at.% Co-61at.% Ir), 1.95 (34at.% Co-66at.% Ir) and 2.2 (31at.% Co-69at. %Ir) for $Co_{1-x}(Ir_x)$ (x=0.2, 0.3, 0.4), respectively, which suggests a significant solute (Ir) segregation on the surface of the alloy nanoparticles. The surface composition of $Co_{1-x}(Ir_x)$ determined from XPS analysis is tabulated in **Table 1**. The enrichment of iridium on the surface of the nanocrystalline $Co_{1-x}(Ir_x)$ metal catalyst over cobalt is a result of heat treatment of all the synthesized alloy catalysts in (Ar+6.5% H_2) atmosphere at 200^0C. This can be attributed to higher adsorption enthalpy of hydrogen on Ir than Co which facilitate segregation of iridium on the catalyst surface.[82-84] Similar results have been reported for carbon supported Pd-Co core-shell nanoparticles, where surface segregation was observed in which Pd migrated from the bulk to the surface forming a thin over-layer, due to heat treatment in H_2 atmosphere.[85] This rearrangement of Pd and Co was attributed to the higher adsorption enthalpy of hydrogen and consequently, stronger affinity of hydrogen on Pd than Co. Similar phenomena can therefore be expected to occur in the case of the Co-Ir alloys discussed herein.

4.3.2 Electrochemical characterization of $Co_{1-x}(Ir_x)$

The electrochemical activity of $Co_{1-x}(Ir_x)$ (x=0.2, 0.3, 0.4) solid solution as anode electro-catalysts for PEMFCs has been examined using cyclic voltammetry (CV). The cyclic voltammograms (CVs) of $Co_{1-x}(Ir_x)$ (x = 0.2, 0.3, 0.4) in H_2 saturated 0.5 M H_2SO_4 over the

voltage window of -0.1 V and 1 V, displayed in **Fig. S10**, show well-defined strong hydrogen oxidation peaks similar to that of Ir-NPs and Pt/C (see **Fig. S3**). The anodic part of CV curves (**Fig. S3** and **S10**) (between -0.04 V to 0.08 V *vs* NHE) of HOR in H_2 saturated 0.5 M H_2SO_4 for all of the $Co_{1-x}(Ir_x)$ solid solution of different compositions (x=0.2, 0.3, 0.4, 1) and Pt/C, before and after iR_Ω correction, are shown in **Fig. 8a**. The ohmic resistance (R_Ω) for all of the alloy electro-catalysts was determined from the EIS Nyquist plots, discussed subsequently in the sections below. As shown in the inset of **Fig 8a**, and plotted in **Fig. 8b**, the onset potential of HOR for all of the $Co_{1-x}(Ir_x)$ solid solution (-0.032 V for x=0.2, -0.036 V for x= 0.3 and -0.037 V for x=0.4) is significantly lower than that for pure Ir-NPs (-0.015 V) and the commercially obtained 40% Pt/C electro-catalyst (-0.025 V). This shift in the onset potentials of $Co_{1-x}(Ir_x)$ (x = 0.2, 0.3, 0.4) to values lower than that of pure Ir-NPs and Pt/C clearly suggests that the solid solution $Co_{1-x}(Ir_x)$ exhibit lower reaction polarization in the Tafel step and hence, expectedly, a higher catalytic activity, in comparison to pure Ir-NPs and Pt/C while all having up to 60-80% lower noble metal, Ir content. In addition it can be seen that the onset potential of the $Co_{1-x}(Ir_x)$ solid solution shifts to lower potential with increase in iridium content and reaches a minimum value of ~(-0.037 V) for $Co_{1-x}(Ir_x)$ with x=0.3 and 0.4. This observed lower onset potential for $Co_{1-x}(Ir_x)$ solid solution in comparison to pure Ir-NPs combined with shifting of the onset potential to lower value with increase in Ir content of $Co_{1-x}(Ir_x)$ up to x=0.4 is in accordance with the results from the theoretical study predicting that $Co_{1-x}(Ir_x)$ alloy with x=0.3 and 0.4 will possess minimum reaction polarization and thus, a minimal overall overpotential due to modification of the electronic structure following the favorable interaction of cobalt with iridium.

The overall electrochemical activity of $Co_{1-x}(Ir_x)$ (x=0.2, 0.3, 0.4, 1) and Pt/C towards HOR is evaluated by comparing the current density at ~0 V in iR_Ω corrected anodic part of CV curves (**Fig. S3** and **S10**) (between -0.04 V to 0.08 V *vs* NHE), as shown in **Fig. 8a**. Since 0 V is the standard redox potential for the HOR, high catalytic activity (.i.e., high current density with minimum overpotential) is desired at 0 V. Hence, 0 V is chosen as reference for comparison of the catalytic performance of all the alloy electro-catalysts studied herein. Values of current density at ~0 V of $Co_{1-x}(Ir_x)$ and Pt/C are plotted in **Fig. 8b** and also tabulated in **Table 2**. As shown in **Fig. 8b** and **Table 2**, the current density of $Co_{0.8}(Ir_{0.2})$ corresponding to ~19 m^2/g ECSA is ~0.64 mA/cm^2 at 0 V, which is 17% higher than that of pure Ir-NPs (~0.54 mA/cm^2) of comparable ECSA (~14.5 m^2/g). The higher electrochemical activity of $Co_{0.8}(Ir_{0.2})$ containing only 20 at % nominal Ir in comparison to Ir-NPs is expected due to lower reaction polarization of $Co_{0.8}(Ir_{0.2})$. However, the current density of $Co_{0.8}(Ir_{0.2})$ at ~0 V is 10% lower than Pt/C (0.71 mA/cm^2) which exhibits nearly three-fold higher ECSA (~55.2 m^2/g) than $Co_{0.8}(Ir_{0.2})$. The higher electrochemical activity of Pt/C may arise due to higher ECSA or higher overall reaction kinetics (lower activation polarization) than $Co_{0.8}(Ir_{0.2})$. On the other hand, it should be noted that $Co_{0.6}(Ir_{0.4})$ of comparable ECSA (~56 m^2/g) to Pt/C exhibits the highest current density of ~1.365 mA/cm^2 which is ~156% higher than pure Ir (~0.54 mA/cm^2) and ~92% higher than the state of the art Pt/C (~0.71 mA/cm^2). Similarly, $Co_{0.7}(Ir_{0.3})$ of ~55.6 m^2/g ECSA exhibits ~94 % and ~46% higher current density (~1.037 mA/cm^2) than Ir-NPs and 40% Pt/C, respectively. The higher electrochemical activity of $Co_{0.7}(Ir_{0.3})$ and $Co_{0.6}(Ir_{0.4})$ in comparison to Pt/C of comparable ECSA is expected due to the lower reaction polarization (overpotential) of $Co_{0.7}(Ir_{0.3})$ and $Co_{0.6}(Ir_{0.4})$ as discussed in the earlier section.

Though the onset potentials (reaction polarization) and ECSA of $Co_{1-x}(Ir_x)$ (x=0.3 and 0.4) are comparable, the current density of $Co_{0.6}(Ir_{0.4})$ at 0 V (~1.365 mA/cm^2) is ~32% higher than $Co_{0.7}(Ir_{0.3})$ (~1.037 mA/cm^2), which suggests that the reaction kinetics or activation polarization (charge transfer kinetics) in the Volmer step of $Co_{0.6}(Ir_{0.4})$ are faster than those occurring on $Co_{0.7}(Ir_{0.3})$ electro-catalysts, in spite of comparable ECSA (~56 m^2/g) (**Fig. 5d**). The above results also clearly suggest that the Co-Ir solid solution (x = 0.3 and 0.4), which display similar ECSA to Pt/C system, exhibits a novel atomic/molecular structure leading to better electrochemical performance than the state of the art Pt based electro-catalyst system.

Electrochemical Impedance spectroscopy

To understand the reaction kinetics and charge transfer kinetics (Volmer reaction step) of $Co_{1-x}(Ir_x)$ alloys, electrochemical impedance spectroscopy (EIS) was carried out to study the charge transfer resistance (R_{ct}) at the electro-catalyst/electrolyte interface. The EIS study has also been used to obtain the ohmic resistance (R_Ω) of the $Co_{1-x}(Ir_x)$, Ir-NPs, and Pt/C electro-catalyst system. **Fig. 9** shows the EIS plots of all the $Co_{1-x}(Ir_x)$ (x = 0.2, 0.3, 0.4 and 1) alloys synthesized along with commercially obtained state of the art Pt/C, obtained at ~0.016 V (*vs* NHE) in the frequency range of 100 mHz-100 kHz. A well-formed semicircular arc is observed at the high frequency range in the EIS plot (**Fig. 9**). The diameter of this arc is typically a measure of the charge transfer resistance (R_{ct}). The R_Ω and R_{ct} of $Co_{1-x}(Ir_x)$ and Pt/C, obtained from fitting the data to an equivalent circuit model of $R_\Omega(R_{ct}Q_1W_o)$ is tabulated in **Table 3**. As shown in **Table 3**, R_{ct} value decreases expectedly with increase in iridium content suggesting a decrease in the electrochemical activation polarization in the Volmer step with increase in Ir content up to

$Co_{0.6}(Ir_{0.4})$. This indicates that there is an enhancement in the electrochemical Faradaic charge-transfer kinetics in addition to the theoretically predicted improvement in reaction polarization and catalytic activity with increase in iridium content up to $Co_{0.6}(Ir_{0.4})$. The R_{ct} of $Co_{0.6}(Ir_{0.4})$ (~5 Ωcm^2) is almost two fold lower than $Co_{0.7}(Ir_{0.3})$ (~12 Ωcm^2) and Pt/C (~13 Ωcm^2) while at the same time being five-fold lower than the chemically synthesized Ir-NPs (~24 Ωcm^2) and $Co_{0.8}(Ir_{0.2})$ (~23.5 Ωcm^2), which explains the lower electrochemical activation polarization resistance and hence, improved electrochemical activity of $Co_{0.6}(Ir_{0.4})$, in comparison to the other alloy $Co_{1-x}(Ir_x)$ (x=0.2, 0.3 and 1) compositions, and Pt/C (**Table 3**).

On the other hand, the measured Tafel slope from Tafel polarization plot of of $Co_{1-x}(Ir_x)$ shows decreasing trend with increase in Ir content upto $Co_{0.6}(Ir_{0.4})$ (**Table 3**). The Tafel slope of $Co_{1-x}(Ir_x)$ (x=0.2, 0.3, 0.4, 1), calculated from iR_Ω corrected Tafel plots shown in **Figs. S4, S11, S12** and **S13** are 71.6, 65.5, 64.2 and 72 mV/dec, respectively, whereas the Tafel slope of Pt/C is ~67 mV/dec (**Fig. S5**). The decrease in Tafel slope with increasing Ir content up to $Co_{0.6}(Ir_{0.4})$ suggests the increase in the number of electrons produced in the HOR processes with increase in iridium content. The above results also clearly show that $Co_{0.6}(Ir_{0.4})$ is indeed a promising anode electro-catalyst for PEMFC due to the lowest reaction and activation polarization and higher ECSA reflected in the observed improvement in electrochemical reaction kinetics. The improved electrochemical activity of $Co_{0.6}(Ir_{0.4})$ in comparison to Pt based system could be correlated with electronic and atomic structure of Co-Ir system as discussed earlier. A fundamental understanding of the atomic level structure and correlation with electrochemical performance will however be helpful to develop the non-noble metal based electro-catalyst.

Rotating disk electrode

In order to study the inherent kinetics of the electrochemical reaction, polarization studies were performed using the rotating disk electrode (RDE). The current at ~0 V typically selected as the voltage for assessing the electrochemical activity prowess of the electro-catalyst is considered in the Koutechy-Levich equation to calculate 'n' for all the tested alloy catalysts. The intercept on the y-axis of the Koutechy-Levich plot is used to determine the kinetic current (i_k), which is the current obtained in the absence of mass transfer limitation. The polarization curve of a representative electro-catalyst, $Co_{0.6}(Ir_{0.4})$ for ω = 100, 400, 900, 1600 and 2500 rpm are shown in **Fig. 10**. The corresponding Koutechy-Levich plot for $Co_{0.6}(Ir_{0.4})$ is also shown in the inset in **Fig. 10**. Values of n and i_k, calculated from the slope and intercept of graph of i^{-1} versus $\omega^{-1/2}$, for all the tested alloy catalysts are given in **Table 4**. The value of n for all the alloy catalysts is close to the theoretical value, .i.e., 2, which implies that the reaction proceeds corresponding to the well-known two electron reaction pathway.

The polarization and Koutechy-Levich plots for the other alloy compositions of $Co_{1-x}(Ir_x)$ (x=0.2, 0.3, 1) and Pt/C, for ω = 100, 400, 900, 1600 and 2500 rpm are shown in the supporting information (**Figs. S14-S17**). It is noteworthy that both 'n' and 'i_k' increase with increase in iridium content of the alloy, which is consistent with the decreasing trend observed in the Tafel slope with increase in iridium content. Thus $Co_{0.6}(Ir_{0.4})$ exhibits the highest i_k (~4.047 mA/cm^2), which is ~37% higher than 40% Pt/C (~2.95 mA/cm^2) and ~110% higher than that of pure Ir (1.932 mA/cm^2). $Co_{0.7}(Ir_{0.3})$ (~3.035 mA/cm^2) also shows ~3% higher i_k than 40% Pt/C and ~57% higher value compared to pure Ir. Though the kinetic current for $Co_{0.8}(Ir_{0.2})$ is lower than that of Pt/C, the kinetic current and 'n' for $Co_{0.8}(Ir_{0.2})$ are comparable to pure Ir indicating the beneficial role of Ir in improving the catalytic activity of $Co_{0.8}(Ir_{0.2})$, confirming the d-band

center first principles calculations described earlier. Nevertheless, the detailed study outlined above confirms the improved reaction kinetics observed for both $Co_{0.7}(Ir_{0.3})$ and $Co_{0.6}(Ir_{0.4})$ alloys, in comparison to $Co_{0.8}(Ir_{0.2})$, 40%Pt/C and pure Ir. These results also indicate the improved inherent reaction kinetics of the $Co_{0.6}(Ir_{0.4})$ than $Co_{0.7}(Ir_{0.3})$ alloys which is also in accordance with the results from EIS measurement indicating the lower R_{ct} observed for $Co_{0.6}(Ir_{0.4})$ compared to $Co_{0.7}(Ir_{0.3})$ shown in **Fig. 9** and **Table 3**. These results thus suggest that modification of the electronic and crystal structure of hcp Co by the introduction of only 20 at% Ir results in transforming the alloy to the fcc form while also rendering it catalytically active towards the hydrogen oxidation reaction for PEMFC application. The study shows clearly how introduction of much reduced amount of Ir not only stabilizes the fcc form of Co but also renders the system more catalytically active than pure Ir nanoparticles as well as the state of the art Pt/C system demonstrating the remarkable potential of these novel alloy forms.

Electrochemical stability/durability test in half cell configuration

While the electrochemical efficacy of these novel alloys has been demonstrated above, it is also imperative to explore and determine the electrochemical stability of these alloy catalysts. Hence to study the robustness of the $Co_{1-x}(Ir_x)$ electro-catalysts during long-term operation in commercial cells, electrochemical stability/durability test of $Co_{1-x}(Ir_x)$ (x=0.2, 0.3, 0.4, 1) has been evaluated for a period of 24 h, the putative expected time frame for determining stability. This is studied by conducting the typically accepted chronoamperometry (CA) analysis for 24 h executed at the constant potential of ~0.016 V (*vs* NHE), which is closer to 0 V (standard redox

potential of HOR). The CA curves of $Co_{1-x}(Ir_x)$ (x=0.2, 0.3, 0.4) are shown in **Fig. 11a**, along with that of commercial Pt/C and the chemically synthesized Ir NPs. The current density is seen to stabilize and become steady after ~2 h of initial testing. For $Co_{0.8}(Ir_{0.2})$, the current drops from ~0.5 mA/cm^2 (after 2 h) to ~0.35 mA/cm^2 (after 24 h), indicating ~30% loss in activity (current density), which is lower than that of pure Ir. Thus, $Co_{0.8}(Ir_{0.2})$ shows superior electrochemical stability than pure Ir, which sheds light on the unique effect of solid-solution alloy formation in improving the catalytic activity for $Co_{0.8}(Ir_{0.2})$ compared to pure Ir, with almost 80% reduction in noble metal content. However, a loss in activity (current density) of only ~5% is observed for both $Co_{0.7}(Ir_{0.3})$ and $Co_{0.6}(Ir_{0.4})$ alloys after 24 h of testing, which is comparable with that of the Pt/C electro-catalyst. For $Co_{0.7}(Ir_{0.3})$, the current density drops from ~1.021 mA/cm^2 (after 2 h) to ~0.971 mA/cm^2 (after 24 h), whereas the current for $Co_{0.6}(Ir_{0.4})$ drops from ~1.254 mA/cm^2 after 2 h to ~1.197 mA/cm^2 after 24 h. Pt/C shows a current density ~0.65 mA/cm^2 after 2 h and ~0.61 mA/cm^2 after 24 h.

On the other hand, the electrochemical activity of pure Ir degrades at a much faster rate (~32.5%, ~0.4 mA/cm^2 after 2 h to ~0.27 mA/cm^2 after 24 h) compared to the Co-Ir alloys. The ICP analysis of the electrolyte collected after 24 h of the electrochemical testing (**Table 5**) shows similar amounts of Ir leached out from the electro-catalyst (~0.04 ppm) irrespective of the composition, whereas the Co amount in the electrolyte increases with increase in Co content in the catalyst layer, such as ~0.359 ppm of Co for $Co_{0.8}(Ir_{0.2})$, ~0.273 ppm of Co for $Co_{0.7}(Ir_{0.3})$ and ~0.162 ppm of Co for $Co_{0.6}(Ir_{0.4})$. The CV curves of HOR for $Co_{1-x}(Ir_x)$ (x=0.2, 0.3, 0.4, 1) along with Pt/C, obtained after 24 h of CA testing are displayed in **Fig. 11(b-c)**. The collected plots clearly show minimal loss in catalytic activity for HOR in comparison to freshly prepared electro-catalyst for $Co_{1-x}(Ir_x)$ (x=0.3, 0.4), likely due to the apparent loss in Co and Ir. However,

significant loss in electrochemical activity for pure Ir is seen, after electrochemical testing for 24 h, in comparison to $Co_{0.8}(Ir_{0.2})$. The results thus demonstrate that although the electrochemical response of these alloys is indeed remarkable there is need for improving the chemical stability of the alloy systems. It is possible to likely improve the durability of Co-Ir based electro-catalyst by introducing more robust and chemically resistant refractory elements into the Co-Ir lattice employing similar chemical reduction and alloying strategies. Deploying such strategies could likely help further chemically stabilize the alloy structure without possibly compromising the electrochemical activity.

Single PEMFC full cell test analysis

The polarization curves of single PEMFC full cell with $Co_{1-x}(Ir_x)$ (x=0.3, 0.4) (total loading of 0.2 mg/cm^2) as anode electro-catalyst and Pt/C as cathode electro-catalyst (0.3 mg of Pt/cm^2) are shown in **Fig. 12 (a-b)**. The polarization curve of Pt/C as anode electro-catalyst (0.2 mg of Pt/cm^2) and Pt/C as cathode electro-catalyst (0.3 mg of Pt/cm^2) with identical loadings is shown in **Fig. 12c** for comparison. For commercial Pt/C, the maximum power density obtained using single PEMFC full cell is ~990 mW/cm^2, which is similar to that reported in other studies.[86] As seen in **Fig. 12 (a-c)**, despite the open circuit potential being identical (0.97 V) for $Co_{1-x}(Ir_x)$ (x=0.3, 0.4) and Pt/C which is also observed in other study,[86] superior electrochemical activity is obtained for $Co_{1-x}(Ir_x)$ (x=0.3, 0.4) compared to Pt/C. The maximum power density obtained using single PEMFC full cell with $Co_{1-x}(Ir_x)$ (x=0.3, 0.4) as anode electro-catalyst is ~1380 mW/cm^2 and ~1830 mW/cm^2, which is ~40% and ~85% higher than that obtained using Pt/C as an anode electro-catalyst (~990 mW/cm^2), respectively (see **Table 2**). The superior electrochemical activity of $Co_{1-x}(Ir_x)$ (x=0.3, 0.4) can be due to lower reaction polarization (**Fig.**

790 **8 a-b**) and lower activation polarization resistance (**Fig. 9**) compared to Pt/C. The polarization
791 curves of single PEMFC using $Co_{1-x}(Ir_x)$ (x=0.3, 0.4) and Pt/C as anode electro-catalyst and Pt/C
792 as cathode electro-catalyst, after 24 h of continuous operation are also shown in **Fig. 12 (a-c)**.
793 Negligible loss in power density is observed for $Co_{1-x}(Ir_x)$ (x=0.3, 0.4) and Pt/C, suggesting
794 excellent electrochemical stability of the $Co_{1-x}(Ir_x)$ (x=0.3, 0.4) catalysts, similar to that of Pt/C.
795 These results therefore suggest that $Co_{1-x}(Ir_x)$ (x=0.3, 0.4) are indeed promising anode electro-
796 catalysts as replacements for Pt/C in PEMFC. The study of stability of electro-catalyst materials
797 in single cell PEMFCs for long term operation (5000 h with cycling, following US-DOE's
798 technical targets) and study of tolerance of PEMFCs for frequent start-stop cycling will be
799 conducted and reported in the near future.[87-89]

800 Nevertheless, the present theoretical and experimental study demonstrates the remarkably
801 improved electro-catalytic performance of $Co_{0.7}(Ir_{0.3})$ and $Co_{0.6}(Ir_{0.4})$ rendering it as a potential
802 candidates for replacement of Pt/C due to its superior electrochemical performance and
803 comparable stability/durability, which is important in the overall goals for identification of
804 alternative electro-catalyst with reduced noble metal content with excellent electrochemical
805 activity and stability to replace Pt/C catalyst for PEMFC. This remarkable improvement in
806 electrochemical performance and also superior electrochemical stability of $Co_{0.7}(Ir_{0.3})$ and
807 $Co_{0.6}(Ir_{0.4})$ as compared to pure Ir-NPs and Pt/C in both half cell configuration and single
808 PEMFC full cell can be attributed to a number of factors as evidenced by the above studies and
809 discussion of the results assayed herein. The modification of the electronic structure due to the
810 interaction of cobalt with the introduction of iridium, as indicated by the first principles d-band
811 center studies and confirmed by XPS analysis, aids in modifying the electronic polarization
812 while reducing the polarization losses as identified by the lower charge transfer resistance in EIS

analysis and lower onset potentials seen in anodic part of CV curve. This is indicative of a lower activation and reaction polarization resulting in improved kinetics as compared to Ir-NPs and Pt/C. In addition, the superior ECSA of the Co-Ir solid-solution catalysts obtained by novel synthesis techniques also facilitates in obtaining superior performance to that of Ir-NPs and Pt/C. The above results clearly show that $Co_{0.7}(Ir_{0.3})$ and $Co_{0.6}(Ir_{0.4})$ are indeed promising electro-catalysts for anode of PEMFC due to their lower activation and reaction polarization reflected in the observed improvement in electrochemical reaction kinetics. The 60-80% reduction in noble metal content with similar/superior electrochemical performance and cycling stability is a remarkable achievement as it represents ~380% improvement in electrochemical performance/noble-metal catalyst content when contrasted with pure Pt/C thus demonstrating a major accomplishment achieved in the gradual progression in advanced research globally conducted towards the development of ultra-low and reduced noble metal containing electro-catalysts for PEMFC applications.

Conclusion

The present study demonstrates a theoretical and experimental study of nanostructured $Co_{1-x}(Ir_x)$ (x=0.2, 0.3, 0.4) solid solution as promising anode electro-catalysts for PEMFC. XRD analyses indicate formation of single phase solid solution for chemically synthesized $Co_{1-x}(Ir_x)$ (x=0.2, 0.3, 0.4) alloy electro-catalysts. The nanostructured alloy electro-catalysts also show uniform distribution of Ir and Co without undergoing any noticeable phase segregation at a specific site. Moreover, $Co_{1-x}(Ir_x)$ (x=0.3 and 0.4) show improved electrochemical performance, ~46% and ~92% improvements in current density compared to Pt/C and ~94% and ~156%

improvements in current density contrasted with pure Ir, respectively. In addition, $Co_{1-x}(Ir_x)$ (x=0.3 and 0.4) show ~40% and ~85% improved maximum power density in single PEMFC study that that of Pt/C. $Co_{1-x}(Ir_x)$ (x=0.3, 0.4) alloys also display excellent electrochemical stability/durability, similar to Pt/C in both half cell configuration and single PEMFC. Using the aid of theoretical first principles electronic structure calculations, a strong correlation between the Ir content and the d-band center positions was established which was also experimentally observed and matched by the overall catalytic activity demonstrated by the Co(Ir) alloys. The computational study detailed herein has clearly demonstrated the crucial effect of the electronic structure peculiarities on the electrochemical activity of the Co(Ir) solid solutions. Hence, the present study demonstrates the use of $Co_{1-x}(Ir_x)$ (x=0.3, 0.4) as potential candidates for replacement of Pt/C due to their superior electrochemical performance and stability/durability. We believe that this work represents an important hallmark in the overall search for non-noble metal based electro-catalysts exhibiting excellent electrochemical activity and stability to replace Pt/C, the currently accepted gold standard catalyst for PEMFC.

Author contribution

P.P.P., O.I.V. and P.N.K. devised the original concept. P.P.P. designed the experiments, synthesized the materials, prepared the electrodes, performed the electrochemical characterization and analyzed electrochemical data. O.I.V. conducted the theoretical analyses. J.P. and A.M. collected and analyzed the XPS data. P.P.P. and D. H. performed SEM and TEM analyses, respectively. M.K.D. and P.J made important suggestions in the context of fundamental structural characterization and electrochemistry. P. P. P., P. J., M.K.D., O.I.V. and P.N.K. wrote

the first draft of the paper; and all authors participated in the manuscript revision. The project is conceived and supervised by P.N.K.

Acknowledgment

Research in part supported by the National Science Foundation, CBET – Grant 0933141. PNK also acknowledges the Edward R. Weidlein Chair Professorship funds and the Center for Complex Engineered Multifunctional Materials (CCEMM) for support of this research and also for procurement of the electrochemical equipment and facilities used in this research work.

References

1. C. Liu, F. Li, L.-P. Ma and H.-M. Cheng, *Advanced Materials*, 2010, 22, E28-E62.
2. J. R. Miller, *Science*, 2012, 335, 1312-1313.
3. B. Peng and J. Chen, *Coordination Chemistry Reviews*, 2009, 253, 2805-2813.
4. P. García, J. P. Torreglosa, L. M. Fernández and F. Jurado, *Expert Systems with Applications*, 2013, 40, 4791-4804.
5. M. K. Debe, *Nature*, 2012, 486, 43-51.
6. M. Ball, M. Wietschel and O. Rentz, *International Journal of Hydrogen Energy*, 2007, 32, 1355-1368.
7. G. Brumfiel, *Nature*, 2003, 422, 104-104.
8. R. Masel, *Nature*, 2006, 442, 521+.
9. C.-J. Winter, *International Journal of Hydrogen Energy*, 2009, 34, S1-S52.

10. C. Yang, P. Costamagna, S. Srinivasan, J. Benziger and A. B. Bocarsly, *Journal of Power Sources*, 2001, 103, 1-9.

11. L. Barreto, A. Makihira and K. Riahi, *International Journal of Hydrogen Energy*, 2003, 28, 267-284.

12. X. G. Yang and C. Y. Wang, *Appl. Phys. Lett.*, 2005, 86, -.

13. M. Oezaslan, F. Hasché and P. Strasser, *The Journal of Physical Chemistry Letters*, 2013, 4, 3273-3291.

14. J. Chen, Y. Li, Z. Gao, G. Wang, J. Tian, C. Jiang, S. Zhu and R. Wang, *Electrochemistry Communications*, DOI: http://dx.doi.org/10.1016/j.elecom.2013.10.001.

15. A. Chandan, M. Hattenberger, A. El-kharouf, S. Du, A. Dhir, V. Self, B. G. Pollet, A. Ingram and W. Bujalski, *Journal of Power Sources*, 2013, 231, 264-278.

16. Z. Liu, L. Ma, J. Zhang, K. Hongsirikarn and J. G. Goodwin, *Catalysis Reviews*, 2013, 55, 255-288.

17. B. Li, D. C. Higgins, D. Yang, H. Lv, Z. Yu and J. Ma, *International Journal of Hydrogen Energy*, 2013, 38, 5813-5822.

18. J. Qiao, B. Li and J. Ma, *Journal of The Electrochemical Society*, 2009, 156, B436-B440.

19. F. Silva, V. Dalmazzo, M. Becker, M. Souza, R. Souza and E. A. Martini, *Ionics*, 2013, DOI: 10.1007/s11581-013-0977-z, 1-8.

20. L. G. S. Pereira, V. A. Paganin and E. A. Ticianelli, *Electrochimica Acta*, 2009, 54, 1992-1998.

21. Y. Dai, Y. Liu and S. Chen, *Electrochimica Acta*, 2013, 89, 744-748.

22. M. Götz and H. Wendt, *Electrochimica Acta*, 1998, 43, 3637-3644.

23. J. E. Hu, Z. Liu, B. W. Eichhorn and G. S. Jackson, *International Journal of Hydrogen Energy*, 2012, 37, 11268-11275.

24. M. Nagarajan, G. Paruthimal kalaignan and G. A. Pathanjali, *International Journal of Hydrogen Energy*, 2011, 36, 14829-14837.

25. D. Ham, S. Han, C. Pak, S. Ji, S.-A. Jin, H. Chang and J. Lee, *Top Catal*, 2012, 55, 922-930.

26. M. P. Humbert, C. A. Menning and J. G. Chen, *Journal of Catalysis*, 2010, 271, 132-139.

27. A. J. Bard, *Journal of Photochemistry*, 1979, 10, 59-75.

28. A. J. Bard and M. A. Fox, *Accounts of Chemical Research*, 1995, 28, 141-145.

29. J. Tayal, B. Rawat and S. Basu, *International Journal of Hydrogen Energy*, 2011, 36, 14884-14897.

30. J. Xu, X. Liu, Y. Chen, Y. Zhou, T. Lu and Y. Tang, *Journal of Materials Chemistry*, 2012, 22, 23659-23667.

31. M. K. Jeon and P. J. McGinn, *Journal of Power Sources*, 2010, 195, 2664-2668.

32. M. K. Jeon and P. J. McGinn, *Journal of Power Sources*, 2009, 188, 427-432.

33. R. S. Amin, R. M. Abdel Hameed, K. M. El-Khatib, H. El-Abd and E. R. Souaya, *International Journal of Hydrogen Energy*, 2012, 37, 18870-18881.

34. Y. M. Alyousef, M. K. Datta, K. Kadakia, S. C. Yao and P. N. Kumta, *Journal of Alloys and Compounds*, 2010, 506, 698-702.

35. Y. M. Alyousef, M. K. Datta, S. C. Yao and P. N. Kumta, *Journal of Physics and Chemistry of Solids*, 2009, 70, 1019-1023.

36. J. Y. Kim, Z. G. Yang, C.-C. Chang, T. I. Valdez, S. R. Narayanan and P. N. Kumta, *Journal of The Electrochemical Society*, 2003, 150, A1421-A1431.

37. K. S. Kadakia, M. K. Datta, O. I. Velikokhatnyi, P. J. Hanumantha, S. K. Park, S. J. Chung, D. H. Hong, J. A. Poston, A. Manivanan and P. N. Kumta, *Journal of The Electrochemical Society*, 2014, 161, F1053-F1060.

38. L. Cao, G. Sun, H. Li and Q. Xin, *Electrochemistry Communications*, 2007, 9, 2541-2546.

39. K. Lee, L. Zhang and J. Zhang, *Journal of Power Sources*, 2007, 170, 291-296.

40. D. Yang, B. Li, H. Zhang and J. Ma, *International Journal of Hydrogen Energy*, 2012, 37, 2447-2454.

41. K. Gong, W.-F. Chen, K. Sasaki, D. Su, M. B. Vukmirovic, W. Zhou, E. L. Izzo, C. Perez-Acosta, P. Hirunsit, P. B. Balbuena and R. R. Adzic, *Journal of Electroanalytical Chemistry*, 2010, 649, 232-237.

42. X. Wang, Y. Tang, Y. Gao and T. Lu, *Journal of Power Sources*, 2008, 175, 784-788.

43. Y. Takasu, N. Yoshinaga and W. Sugimoto, *Electrochemistry Communications*, 2008, 10, 668-672.

44. K. Kadakia, M. K. Datta, O. I. Velikokhatnyi, P. Jampani, S. K. Park, P. Saha, J. A. Poston, A. Manivannan and P. N. Kumta, *International Journal of Hydrogen Energy*, 2012, 37, 3001-3013.

45. M. K. Datta, K. Kadakia, O. I. Velikokhatnyi, P. H. Jampani, S. J. Chung, J. A. Poston, A. Manivannan and P. N. Kumta, *Journal of Materials Chemistry A*, 2013, 1, 4026-4037.

46. K. Kadakia, M. K. Datta, O. I. Velikokhatnyi, P. Jampani, S. K. Park, S. J. Chung and P. N. Kumta, *Journal of Power Sources*, 2014, 245, 362-370.

47. K. Kadakia, M. K. Datta, O. I. Velikokhatnyi, P. H. Jampani and P. N. Kumta, *International Journal of Hydrogen Energy*, 2014, 39, 664-674.

48. K. S. Kadakia, P. H. Jampani, O. I. Velikokhatnyi, M. K. Datta, S. K. Park, D. H. Hong, S. J. Chung and P. N. Kumta, *Journal of Power Sources*, 2014, 269, 855-865.

49. B. Li, D. C. Higgins, D. Yang, R. Lin, Z. Yu and J. Ma, *International Journal of Hydrogen Energy*, 2012, 37, 18843-18850.

50. B. Li, J. Qiao, D. Yang, J. Zheng, J. Ma, J. Zhang and H. Wang, *Electrochimica Acta*, 2009, 54, 5614-5620.

51. D. Yang, B. Li, H. Zhang and J. Ma, *Fuel Cells*, 2013, 13, 309-313.

52. Platinum today, http://platinum.matthey.com/prices/price-tables, Accessed Nov 8, 2013.

53. G. Kresse and J. Furthmüller, *Physical Review B*, 1996, 54, 11169.

54. G. Kresse and J. Furthmüller, *Computational Materials Science*, 1996, 6, 15-50.

55. G. Kresse and D. Joubert, *Physical Review B*, 1999, 59, 1758.

56. B. Wang, J. Iqbal, X. Shan, G. Huang, H. Fu, R. Yu and D. Yu, *Materials Chemistry and Physics*, 2009, 113, 103-106.

57. J. P. Perdew and W. Yue, *Physical Review B*, 1986, 33, 8800.

58. R. Lin, C. Cao, T. Zhao, Z. Huang, B. Li, A. Wieckowski and J. Ma, *Journal of Power Sources*, 2013, 223, 190-198.

59. Y.-C. Hsieh, Y. Zhang, D. Su, V. Volkov, R. Si, L. Wu, Y. Zhu, W. An, P. Liu, P. He, S. Ye, R. R. Adzic and J. X. Wang, *Nature communications*, 2013, 4, 2466-2466.

60. T. H. de Keijser, J. I. Langford, E. J. Mittemeijer and A. B. P. Vogels, *Journal of Applied Crystallography*, 1982, 15, 308-314.

61. T. Vidakovic-Koch, Otto-von-Guericke-Universität Magdeburg, Germany, 2005.

62. R. Jiang and D. Chu, *Electrochimica acta*, 2000, 45, 4025-4030.

63. C. N. Singman, *Journal of Chemical Education*, 1984, 61, 137.

64. B. Seger and P. V. Kamat, *The Journal of Physical Chemistry C*, 2009, 113, 7990-7995.

65. L. Xiong and A. Manthiram, *Electrochimica Acta*, 2004, 49, 4163-4170.

66. B. E. Conway and B. V. Tilak, *Electrochimica Acta*, 2002, 47, 3571-3594.

67. Y. Sun, Y. Dai, Y. Liu and S. Chen, *Physical Chemistry Chemical Physics*, 2012, 14, 2278-2285.

68. T. Bligaard and J. K. Nørskov, *Electrochimica Acta*, 2007, 52, 5512-5516.

69. B. Hammer and J. K. Nørskov, *Advances in catalysis*, 2000, 45, 71-129.

70. H. Okamoto, *Desk handbook: phase diagrams for binary alloys*, ASM international, 2000.

71. A. Fernández Guillermet, *Int J Thermophys*, 1987, 8, 481-510.

72. B. S. Murty, M. K. Datta and S. K. Pabi, *Sadhana*, 2003, 28, 23-45.

73. S. Ram, *Acta Materialia*, 2001, 49, 2297-2307.

74. A. Luo, K. S. Shin and D. L. Jacobson, *AIP Conference Proceedings*, 1991, 217, 334-346.

75. R. Nyholm, A. Berndtsson and N. Martensson, *Journal of Physics C: Solid State Physics*, 1980, 13, L1091.

76. A. Arico, A. Shukla, H. Kim, S. Park, M. Min and V. Antonucci, *Applied Surface Science*, 2001, 172, 33-40.

77. M. Wakisaka, S. Mitsui, Y. Hirose, K. Kawashima, H. Uchida and M. Watanabe, *The Journal of Physical Chemistry B*, 2006, 110, 23489-23496.

78. W. Chen and S. Chen, *Journal of Materials Chemistry*, 2011, 21, 9169-9178.

79. J.-H. Choi, K.-W. Park, B.-K. Kwon and Y.-E. Sung, *Journal of The Electrochemical Society*, 2003, 150, A973-A978.

80. K.-W. Park, J.-H. Choi, B.-K. Kwon, S.-A. Lee, Y.-E. Sung, H.-Y. Ha, S.-A. Hong, H. Kim and A. Wieckowski, *The Journal of Physical Chemistry B*, 2002, 106, 1869-1877.

81. A. Mandale, S. Badrinarayanan, S. Date and A. Sinha, *Journal of electron spectroscopy and related phenomena*, 1984, 33, 61-72.

82. N. Popova and L. Babenkova, *Reaction Kinetics and Catalysis Letters*, 1979, 11, 187-192.

83. H. Shi, O. Y. Gutiérrez, G. L. Haller, D. Mei, R. Rousseau and J. A. Lercher, *Journal of Catalysis*, 2013, 297, 70-78.

84. M. Bridge, C. Comrie and R. Lambert, *Journal of Catalysis*, 1979, 58, 28-33.

85. D. Wang, H. L. Xin, H. Wang, Y. Yu, E. Rus, D. A. Muller, F. J. DiSalvo and H. D. Abruña, *Chemistry of Materials*, 2012, 24, 2274-2281.

86. W. Zhang, L. Li, W. Ding, S. Chen, H. Wang and Z. Wei, *Journal of Materials Chemistry A*, 2014, 2, 10098-10103.

87. C. A. Reiser, L. Bregoli, T. W. Patterson, S. Y. Jung, J. D. Yang, M. L. Perry and T. D. Jarvi, *Electrochemical and Solid-State Letters*, 2005, 8, A273-A276.

88. L. Roen, C. Paik and T. Jarvi, *Electrochemical and Solid-State Letters*, 2004, 7, A19-A22.

89. R. Borup, J. Davey, D. Wood, F. Garzon, M. Inbody and D. Guidry, *DOE hydrogen program, FY*, 2005.

Table 1: The lattice parameter, molar volume, particle size, BET surface area, ECSA, composition determined from EDAX, and surface compositions determined from XPS of $Co_{1-x}(Ir_x)$ electro-catalyst

Compositions (x)	Lattice parameter (nm)	Molar volume (cm^3/mol)	Particle size (nm)	ECSA (m^2/g)	BET surface area (m^2/g)	Bulk and surface composition by	
						EDAX (bulk)	XPS (surface)
0.0	a=0.2505 c=0.4071	6.66	32	-	-	-	-

0.2	0.3671	7.02	2.48	19	37.2	82.1 at.% Co- 17.9 at.% Ir-	61.1 at.% Ir- 38.9 at.% Co
0.3	0.3692	7.22	3.61	55.6	64.3	71.4 at.% Co- 28.6 at.% Ir	66.1 at.% Ir- 33.9 at.% Co
0.4	0.3712	7.42	4.21	56.1	68.2	62.2 at.% Co- 37.8 at.% Ir	68.75 at.% Ir- 31.25 at.% Co
1.0	0.3834	8.49	7.59	14.5	29	-	-
Pt/C				55.2	273.2		

Table 2: Results of electrochemical characterization for HOR of $Co_{1-x}(Ir_x)$ and Pt/C in half-cell configuration and single PEMFC

Electro-	**Onset**	**Current**	**Max. power**

catalyst, $Co_{1-x}(Ir_x)$	potential (mV)	density at 0 V (*vs* NHE) (mA/cm^2)	density in single cell PEMFC (mW/cm^2)
x=0.2	-32.1	0.64	-
x=0.3	-36.29	1.04	1380
x=0.4	-37.39	1.36	1830
x=1	-15.06	0.54	-
Pt/C	-25.7	0.71	990

Table 3: Results of EIS analysis of $Co_{1-x}(Ir_x)$ and Pt/C, carried out at ~0.016 V (*vs* NHE) in frequency range of 100 mHz-100 kHz

Electro-catalyst, $Co_{1-x}(Ir_x)$	R_Ω (Ωcm^2)	R_{ct} (Ωcm^2)	Tafel slope (mV/dec)
x=0.2	13.75	23.5	71.6
x=0.3	13.86	11.94	65.5
x=0.4	13.39	5.149	64.2
x=1	14.88	24	72.0
Pt/C	14.54	13	67.2

Table 4: Results of polarization study of $Co_{1-x}(Ir_x)$ and Pt/C on RDE

x	n	Kinetic current, i_k (mA/cm^2)
0.2	1.77	2.179
0.3	1.79	3.035
0.4	1.81	4.047
1.0	1.75	1.932
Pt/C	1.80	2.95

Table 5: Results of ICP analysis conducted on the electrolyte collected after 24 h chronoamperometry analysis, for $Co_{1-x}(Ir_x)$ and Pt/C

x	Co	Ir	Pt
0.2	**0.359**	**0.04**	**-**
0.3	**0.273**	**0.04**	**-**
0.4	**0.162**	**0.04**	**-**
1.0	**-**	**0.04**	**-**
Pt/C	**-**	**-**	**0**

Figure captions

Figure 1: Co-Ir binary equilibrium phase diagram

Figure 2: The XRD pattern of $Co_{1-x}(Ir_x)$ (x=0, 0.2, 0.3, 0.4, 1) nanoparticles in wide angle 2θ scan

Figure 3 The anodic part of CV curve (**Fig. S3**) (between -0.05 V to 0.2 V *vs* NHE) curve for HOR of Ir-NPs and Pt/C, measured in H_2 saturated 0.5 M H_2SO_4 at 40^0C at scan rate of 10 mV/sec, before and after iR_Ω correction

Figure 4: Ir-d band partial DOS of $Co_{1-x}(Ir_x)$ for different Ir concentrations. Arrows denote position of d-band centers ε_d

Figure 5: (a) Variation of molar volume and particle size with iridium content, (b) The bright field TEM image $Co_{0.6}(Ir_{0.4})$ shows the presence of fine particles in the nanometer range (~4-7

nm), (c) The HRTEM image of $Co_{0.6}(Ir_{0.4})$ shows lattice fringes with a spacing of ~0.215 nm, (d) Variation of BET surface area and ECSA with iridium content

Figure 6: SEM micrograph with elemental mapping and EDAX spectrum of $Co_{0.6}(Ir_{0.4})$

Figure 7: The XPS spectra of $Co_{1-x}(Ir_x)$ showing (a) Ir $4f_{5/2}$ and $4f_{7/2}$ doublet and (b) Co $2p_{1/2}$ and $2p_{3/2}$ doublet

Figure 8: (a) The anodic part of CV curve (**Fig. S3** and **S10**) (between -0.04 V to 0.08 V *vs* NHE) curve for HOR of $Co_{1-x}(Ir_x)$ (x=0.2, 0.3, 0.4, 1) and Pt/C with magnified image between -0.04 V to -0.01 V (*vs* NHE) in inset, measured in H_2 saturated 0.5 M H_2SO_4 at 40^0C at scan rate of 10 mV/sec, before and after iR_Ω correction, (b) Variation of onset potential and current (at 0 V *vs* NHE) with iridium content

Figure 9: EIS spectra of $Co_{1-x}(Ir_x)$ (x=0.2, 0.3, 0.4, 1) and Pt/C obtained at ~0.016 V (*vs* NHE) in H_2 saturated 0.5 M H_2SO_4 solution at 40^0C in the frequency range of 100 mHz to 100 kHz

Figure 10: The polarization curve for HOR of $Co_{0.6}(Ir_{0.4})$ obtained on rotating disk electrode (RDE), measured in H_2 saturated 0.5 M H_2SO_4 solution at 40^0C with a scan rate of 10 mV/sec. Koutechy-Levich plot of $Co_{0.6}(Ir_{0.4})$ is shown in inset of polarization curve

Figure 11: (a) The variation of current *vs* time in the chronoamperometry test of $Co_{1-x}(Ir_x)$ (x=0.2, 0.3, 0.4, 1) and Pt/C, performed in H_2 saturated 0.5 M H_2SO_4 solution under a constant potential of ~0.016 V (*vs* NHE) at 40^0C for 24 h, (b) The cyclic voltammetry (CV) curve for HOR of $Co_{1-x}(Ir_x)$ (x=0.2, 0.3, 0.4), measured in H_2 saturated 0.5 M H_2SO_4 at 40^0C at scan rate of 10 mV/sec, obtained after 24 h chronoamperometry test, (c) The cyclic voltammetry (CV) curve for HOR of Ir NPs and Pt/C, measured in H_2 saturated 0.5 M H_2SO_4 at 40^0C at scan rate of 10 mV/sec, obtained after 24 h chronoamperometry test

1084 **Figure 12:** Performance of single PEMFC with (a) $Co_{1-x}(Ir_x)$ (x=0.3) (total loading=0.2 mg/cm^2),
1085 (b) $Co_{1-x}(Ir_x)$ (x=0.4) (total loading=0.2 mg/cm^2) and (c) Pt/C (0.2 mg of Pt/cm^2) as anode
1086 electro-catalyst and Pt/C (0.3 mg of Pt/cm^2) as cathode electro-catalyst at 80^0C and 0.1 MPa with
1087 UHP-H_2 (200 ml/min) and UHP-O_2 (300 ml/min) as reactant gases

1088

1089

1090

1091

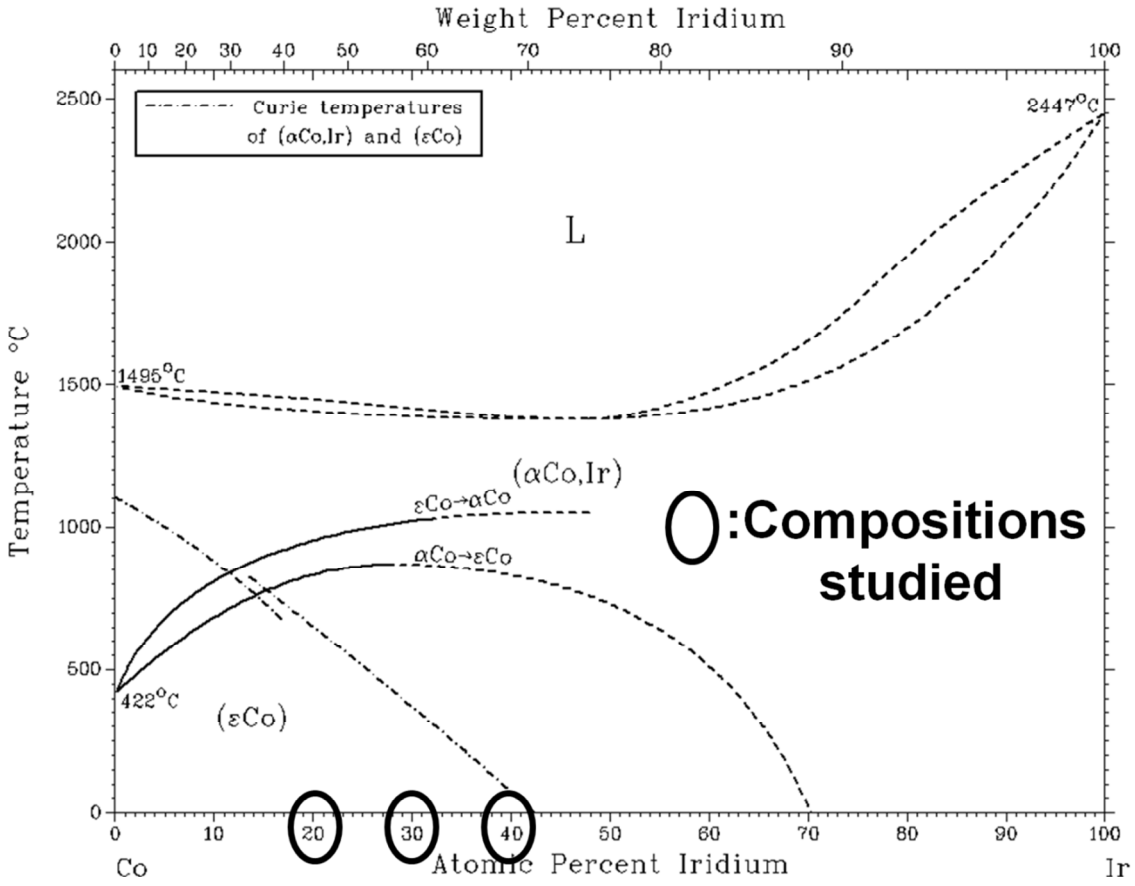

Figure 1: Co-Ir binary equilibrium phase diagram

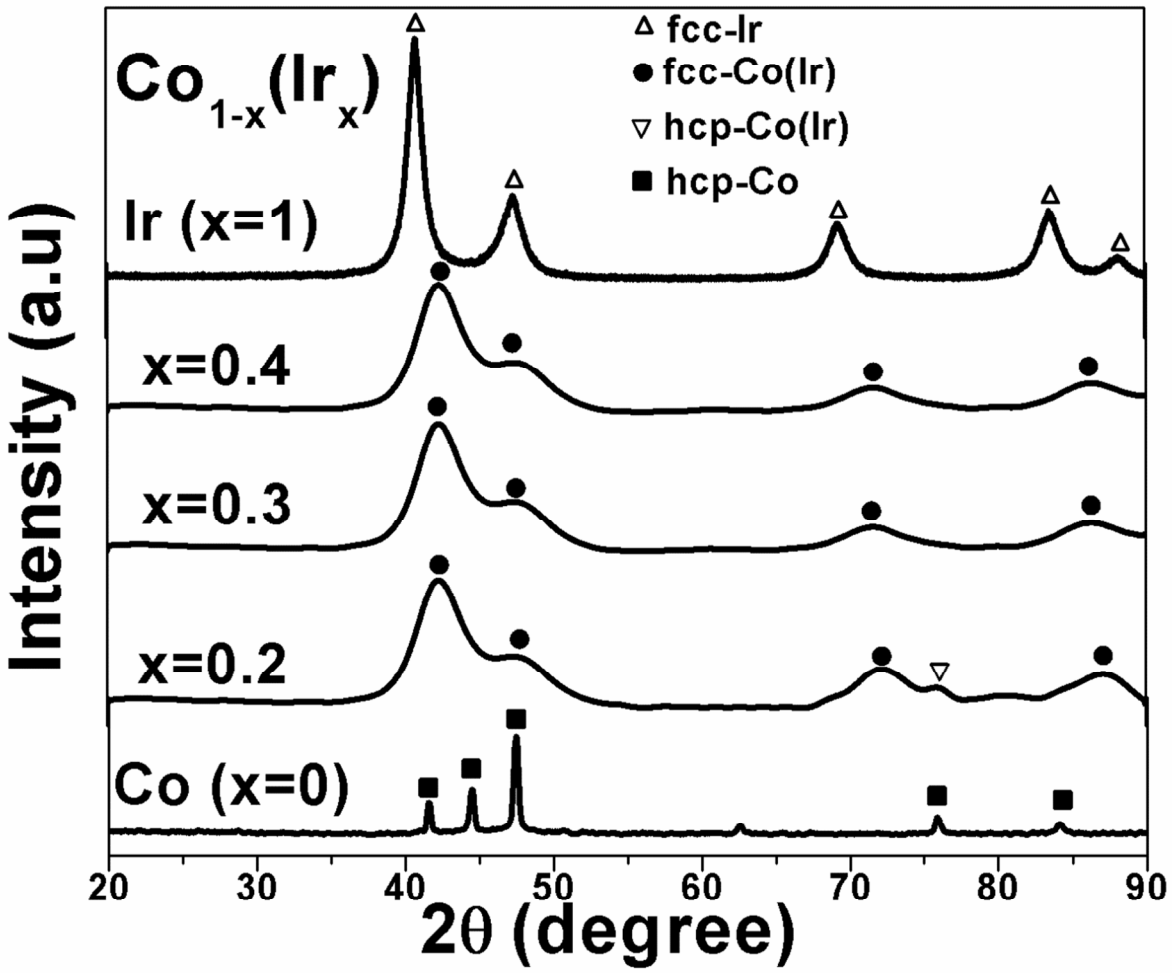

Figure 2: The XRD pattern of $Co_{1-x}(Ir_x)$ (x=0, 0.2, 0.3, 0.4, 1) nanoparticles in wide angle 2θ scan

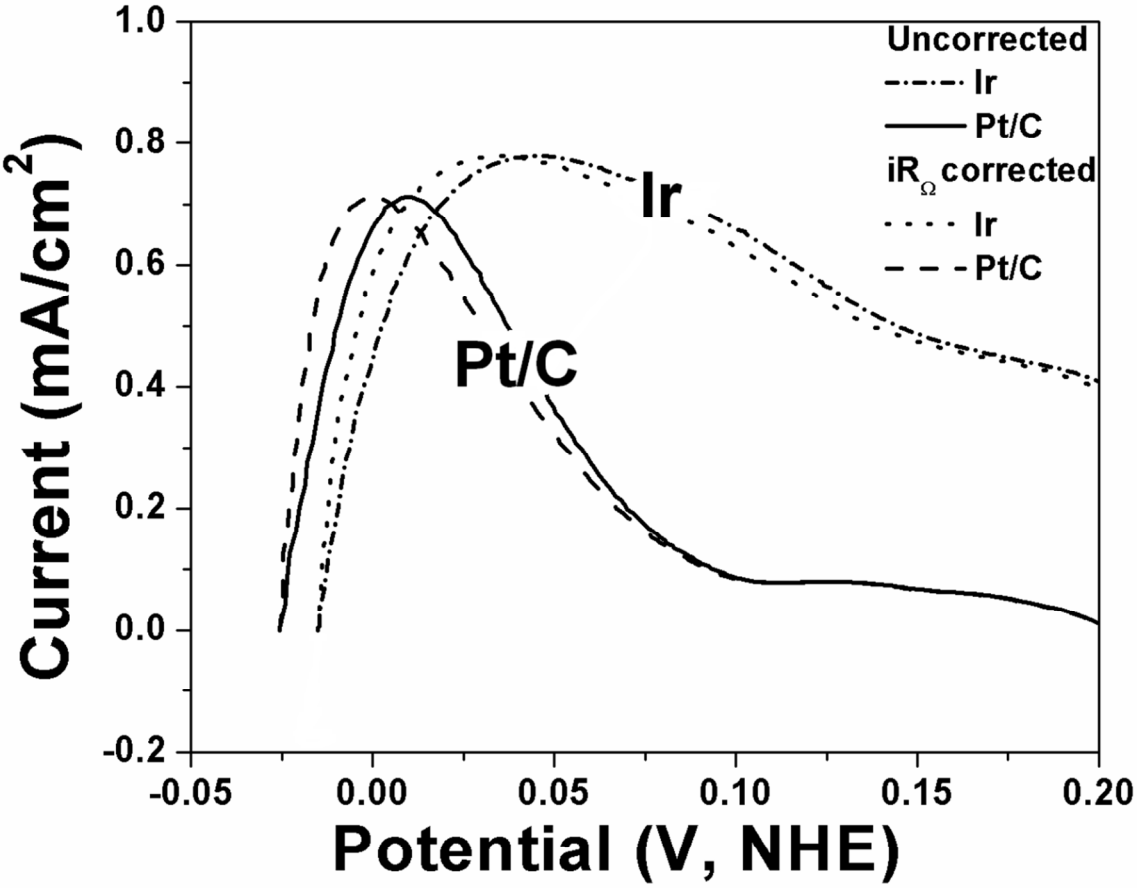

Figure 3 The anodic part of CV curve (**Fig. S3**) (between -0.05 V to 0.2 V *vs* NHE) curve for HOR of Ir-NPs and Pt/C, measured in H_2 saturated 0.5 M H_2SO_4 at 40^0C at scan rate of 10 mV/sec, before and after iR_Ω correction

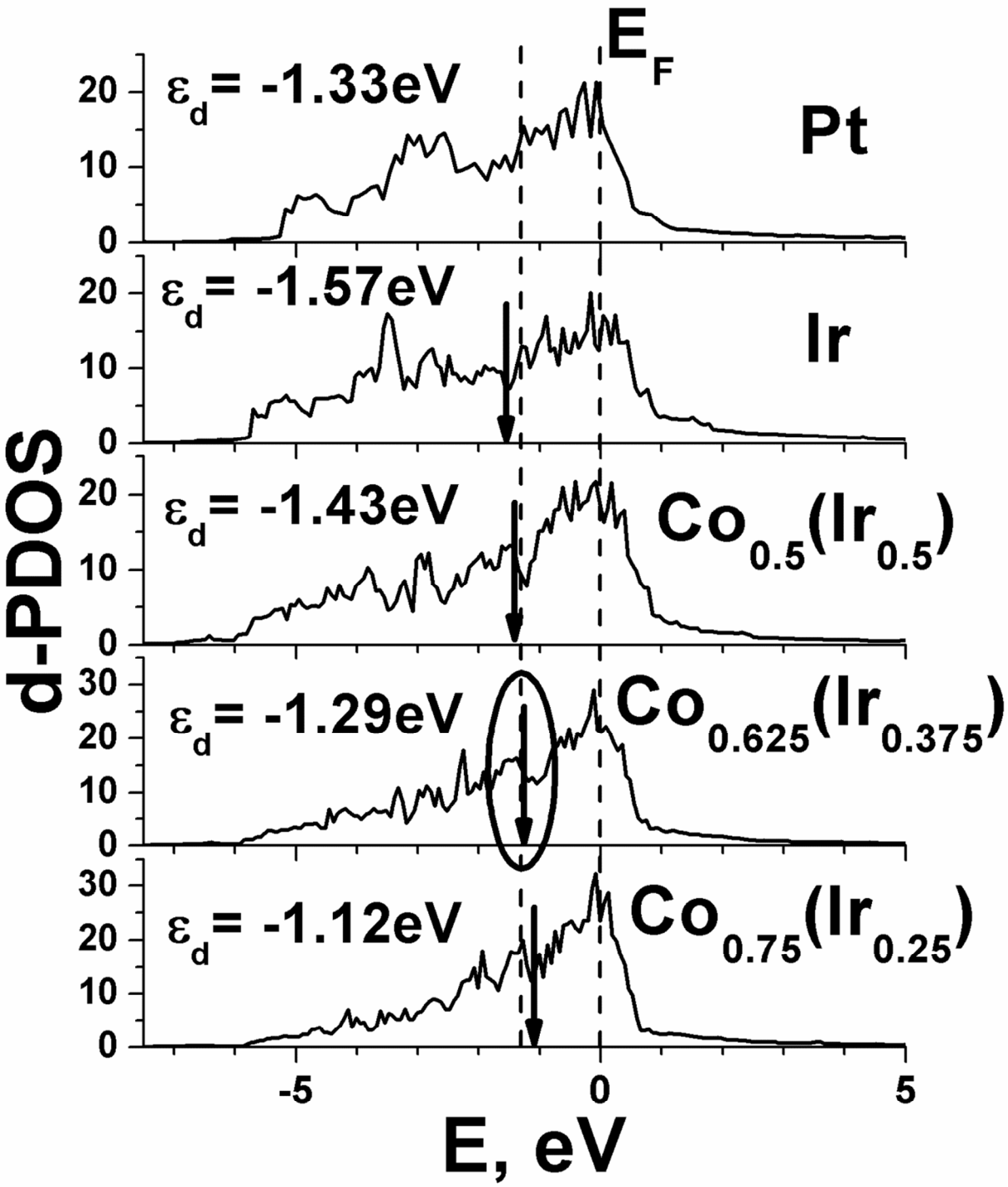

Figure 4: Ir-d band partial DOS of $Co_{1-x}(Ir_x)$ for different Ir concentrations. Arrows denote position of d-band centers ε_d

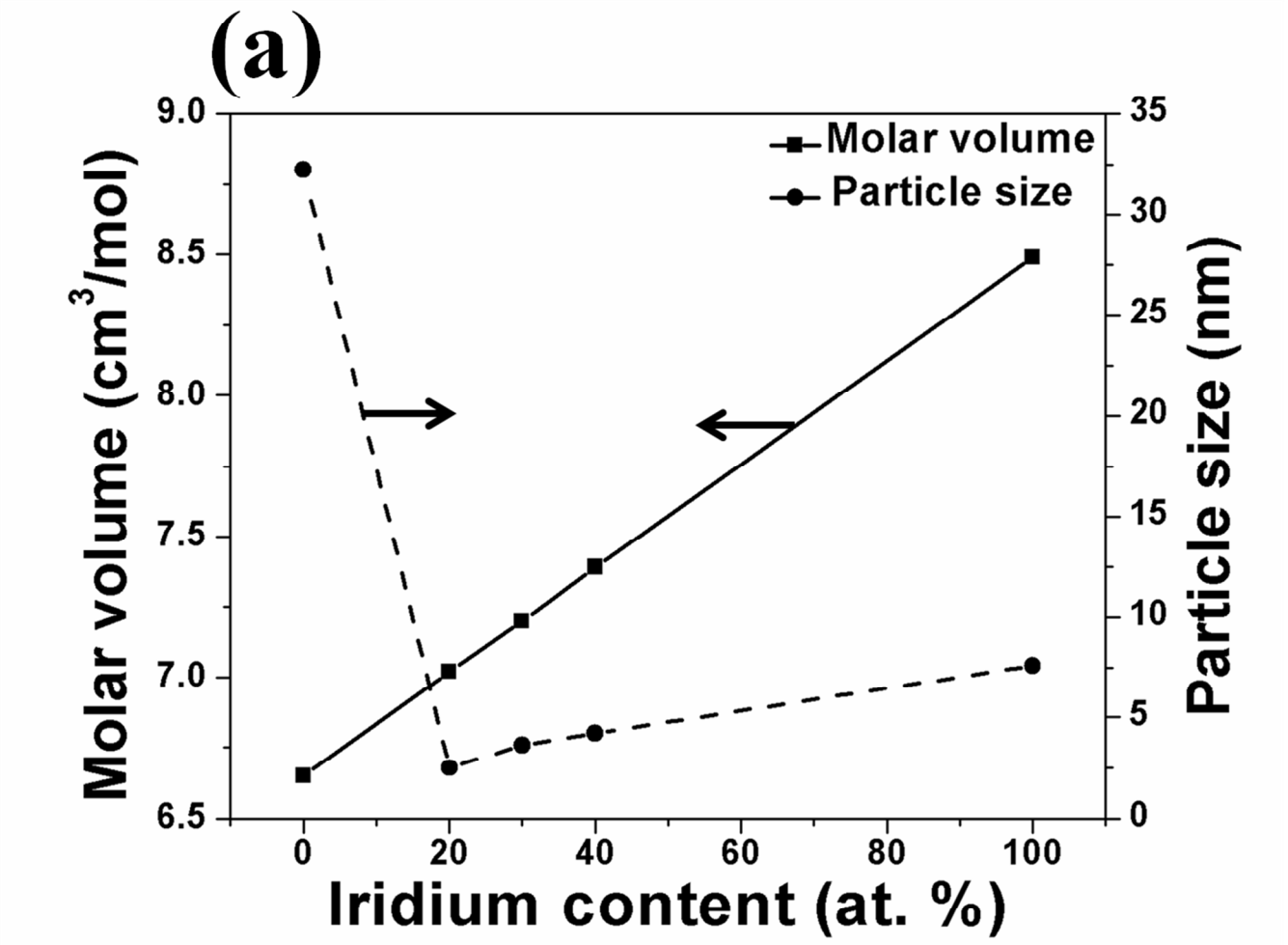

Figure 5: (a) Variation of molar volume and particle size with iridium content, (b) The bright field TEM image $Co_{0.6}(Ir_{0.4})$ shows the presence of fine particles in the nanometer range (~4-7 nm), (c) The HRTEM image of $Co_{0.6}(Ir_{0.4})$ shows lattice fringes with a spacing of ~0.215 nm, (d) Variation of BET surface area and ECSA with iridium content

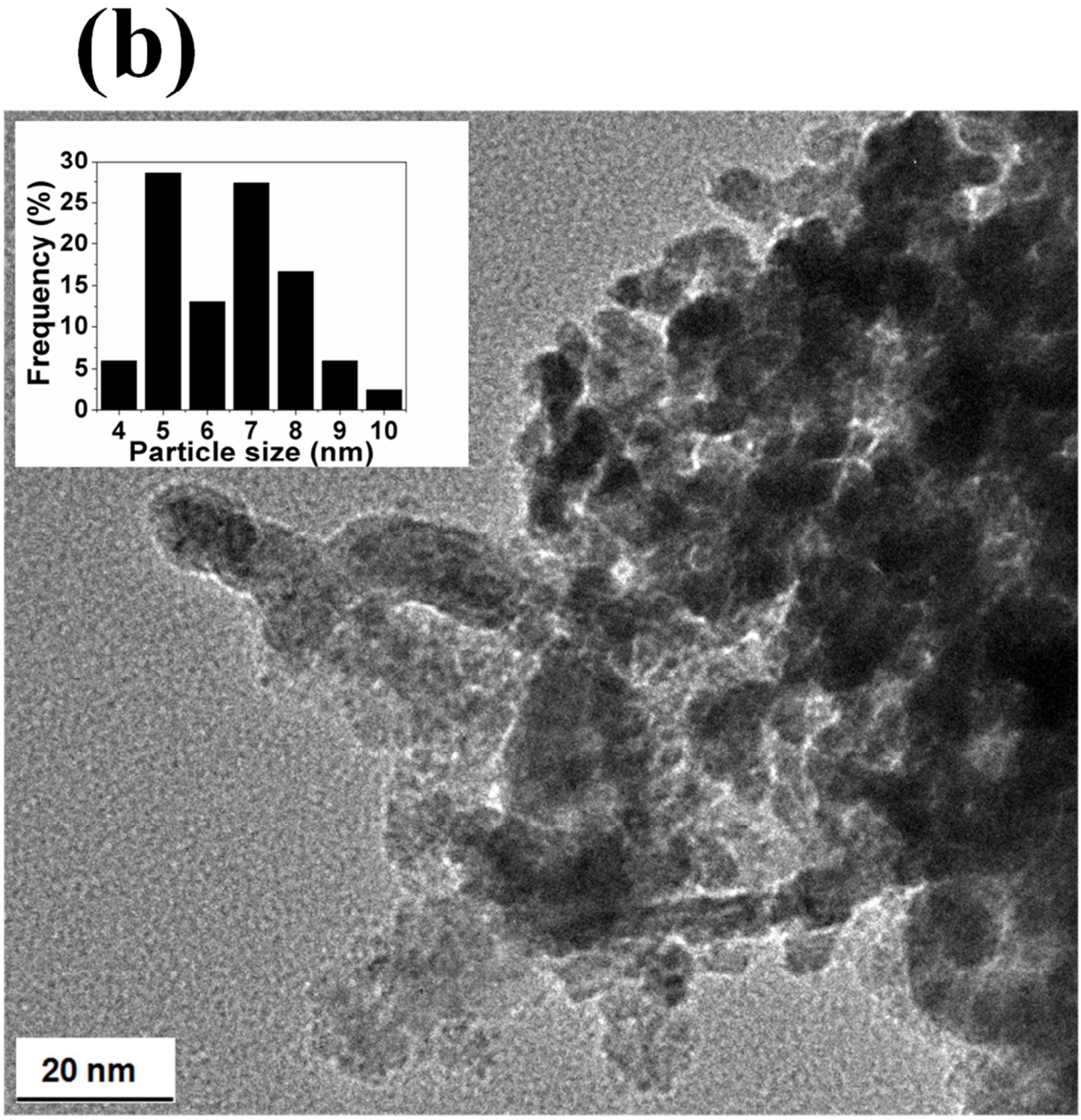

Figure 5: (a) Variation of molar volume and particle size with iridium content, (b) The bright field TEM image $Co_{0.6}(Ir_{0.4})$ shows the presence of fine particles in the nanometer range (~4-7 nm), (c) The HRTEM image of $Co_{0.6}(Ir_{0.4})$ shows lattice fringes with a spacing of ~0.215 nm, (d) Variation of BET surface area and ECSA with iridium content

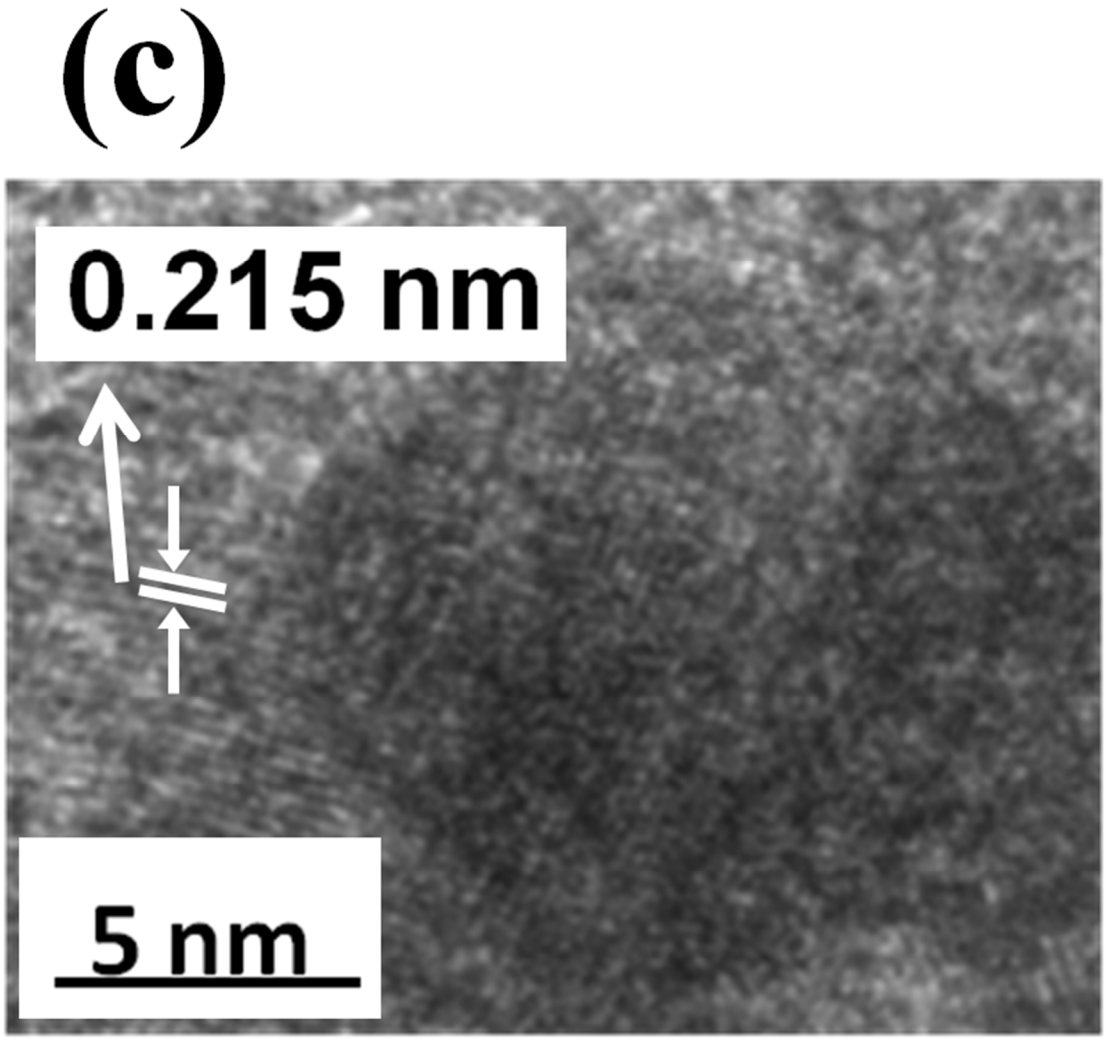

Figure 5: (a) Variation of molar volume and particle size with iridium content, (b) The bright field TEM image $Co_{0.6}(Ir_{0.4})$ shows the presence of fine particles in the nanometer range (~4-7 nm), (c) The HRTEM image of $Co_{0.6}(Ir_{0.4})$ shows lattice fringes with a spacing of ~0.215 nm, (d) Variation of BET surface area and ECSA with iridium content

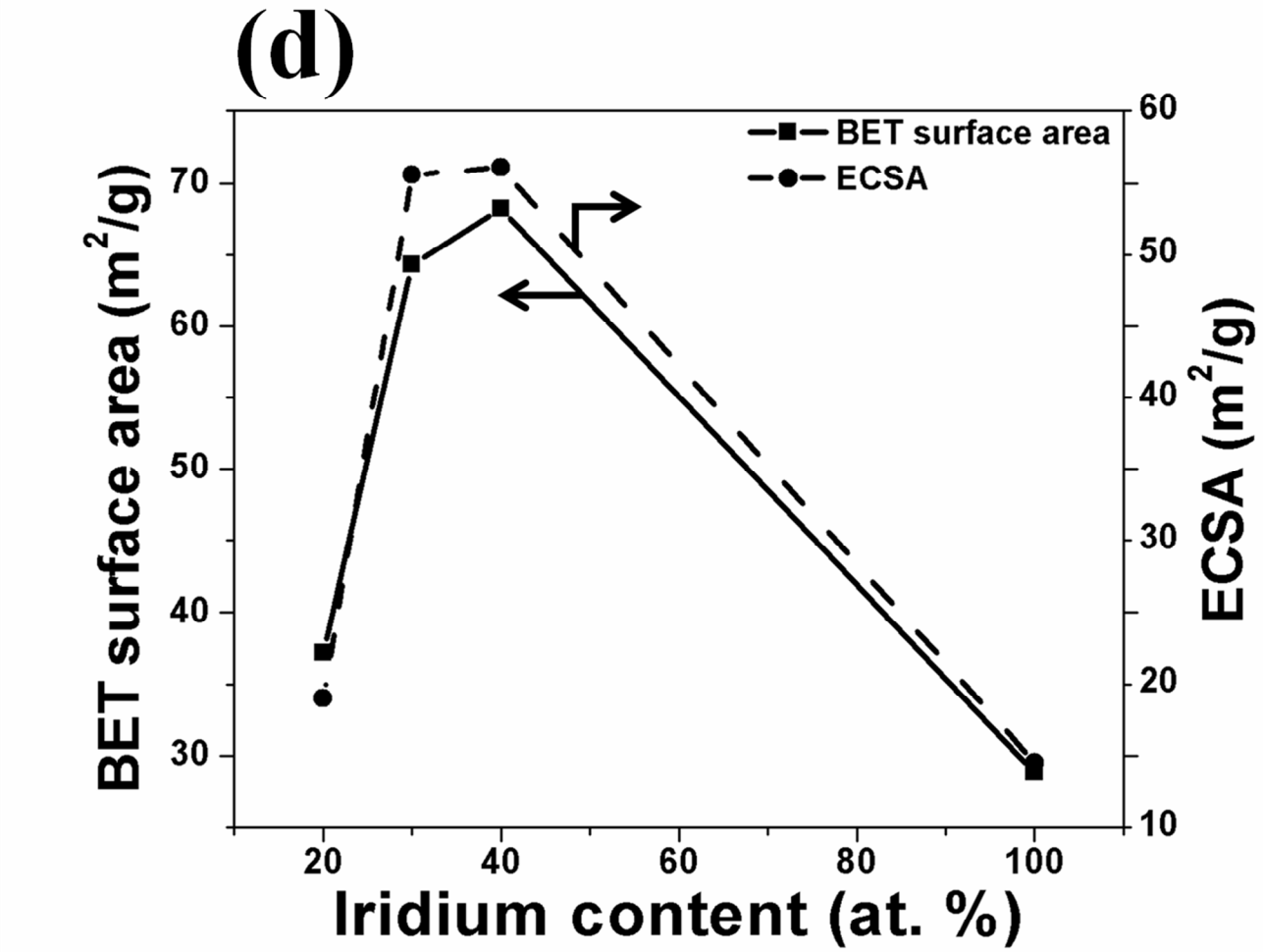

Figure 5: (a) Variation of molar volume and particle size with iridium content, (b) The bright field TEM image $Co_{0.6}(Ir_{0.4})$ shows the presence of fine particles in the nanometer range (~4-7 nm), (c) The HRTEM image of $Co_{0.6}(Ir_{0.4})$ shows lattice fringes with a spacing of ~0.215 nm, (d) Variation of BET surface area and ECSA with iridium content

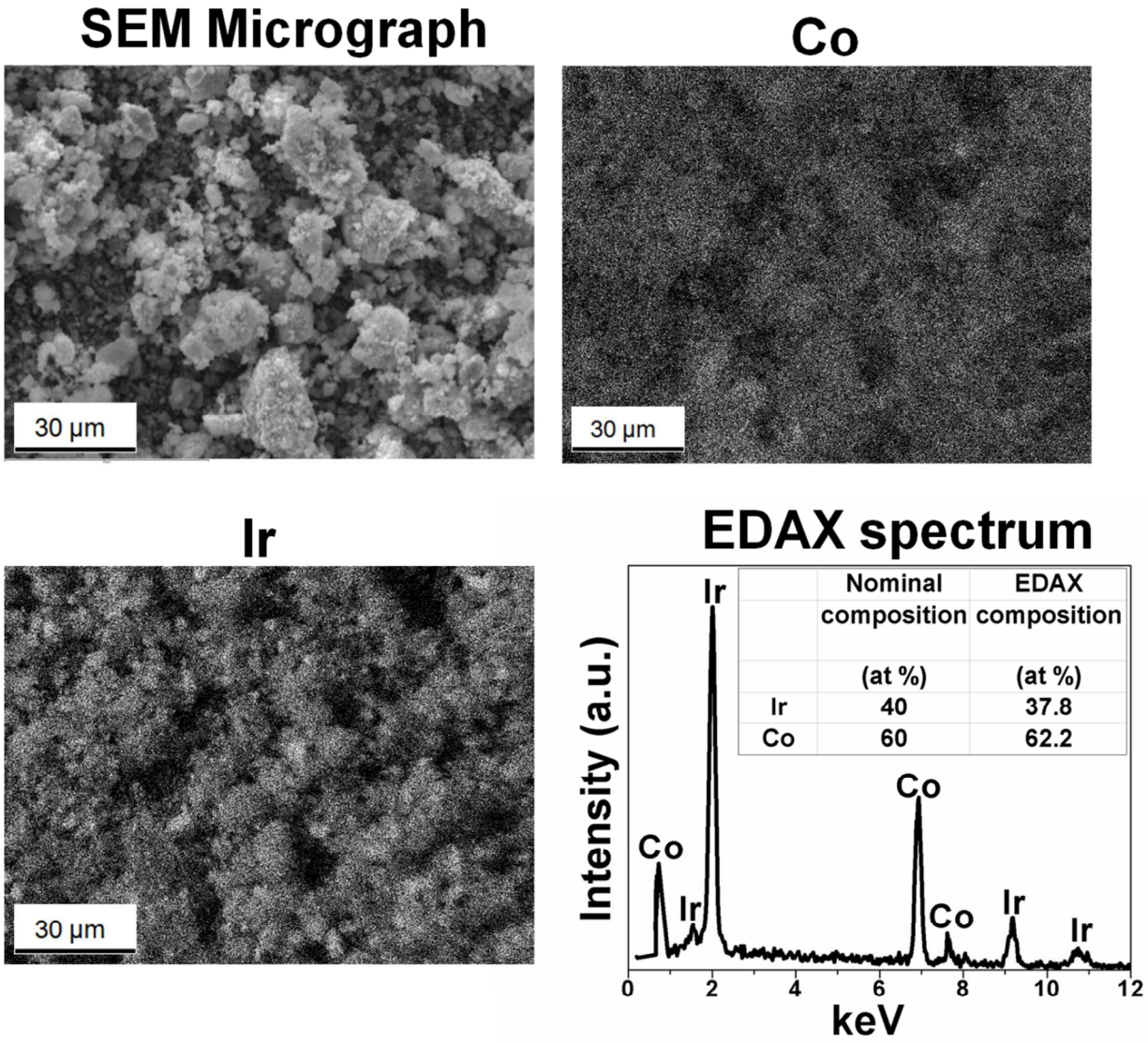

Figure 6: SEM micrograph with elemental mapping and EDAX spectrum of $Co_{0.6}(Ir_{0.4})$

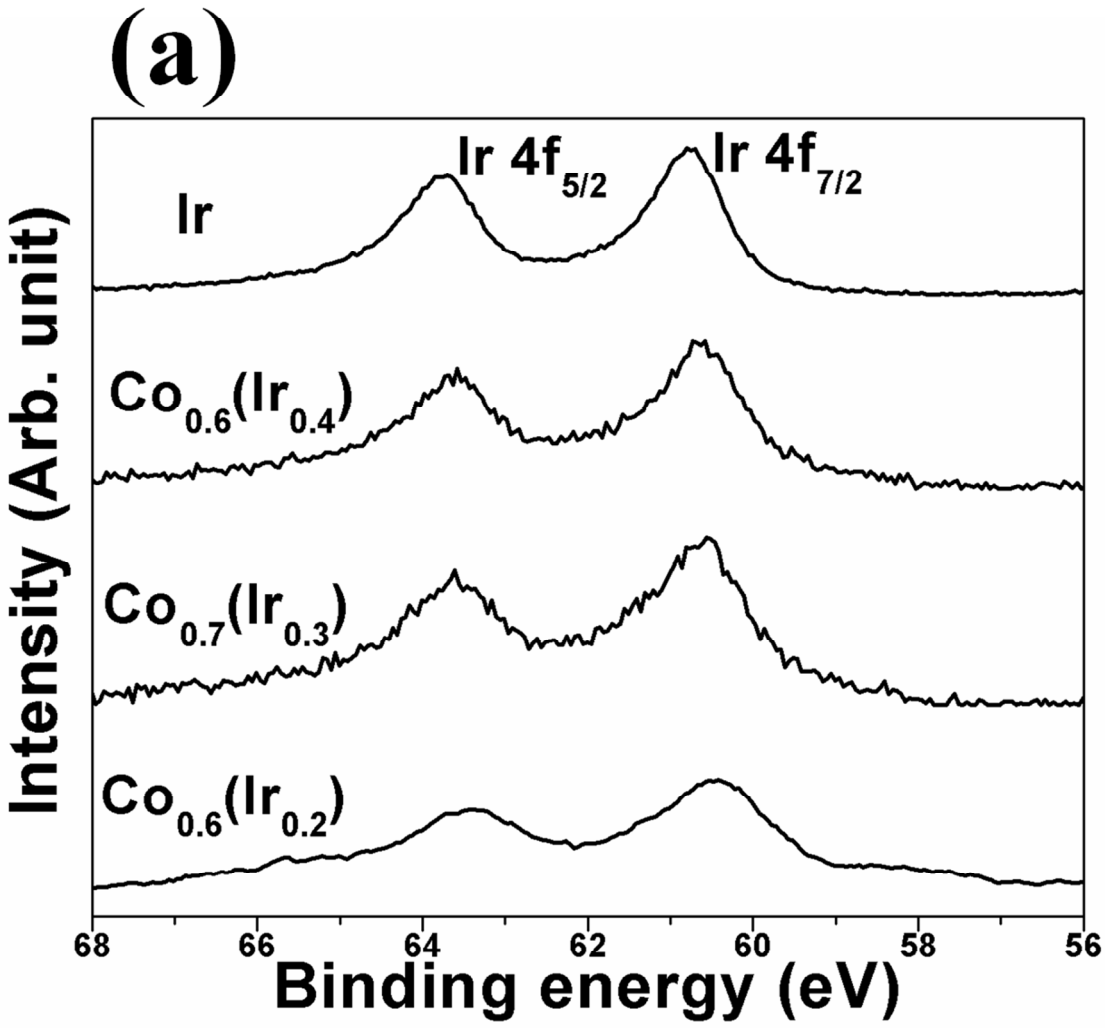

Figure 7: The XPS spectra of $Co_{1-x}(Ir_x)$ showing (a) Ir $4f_{5/2}$ and $4f_{7/2}$ doublet and (b) Co $2p_{1/2}$ and $2p_{3/2}$ doublet

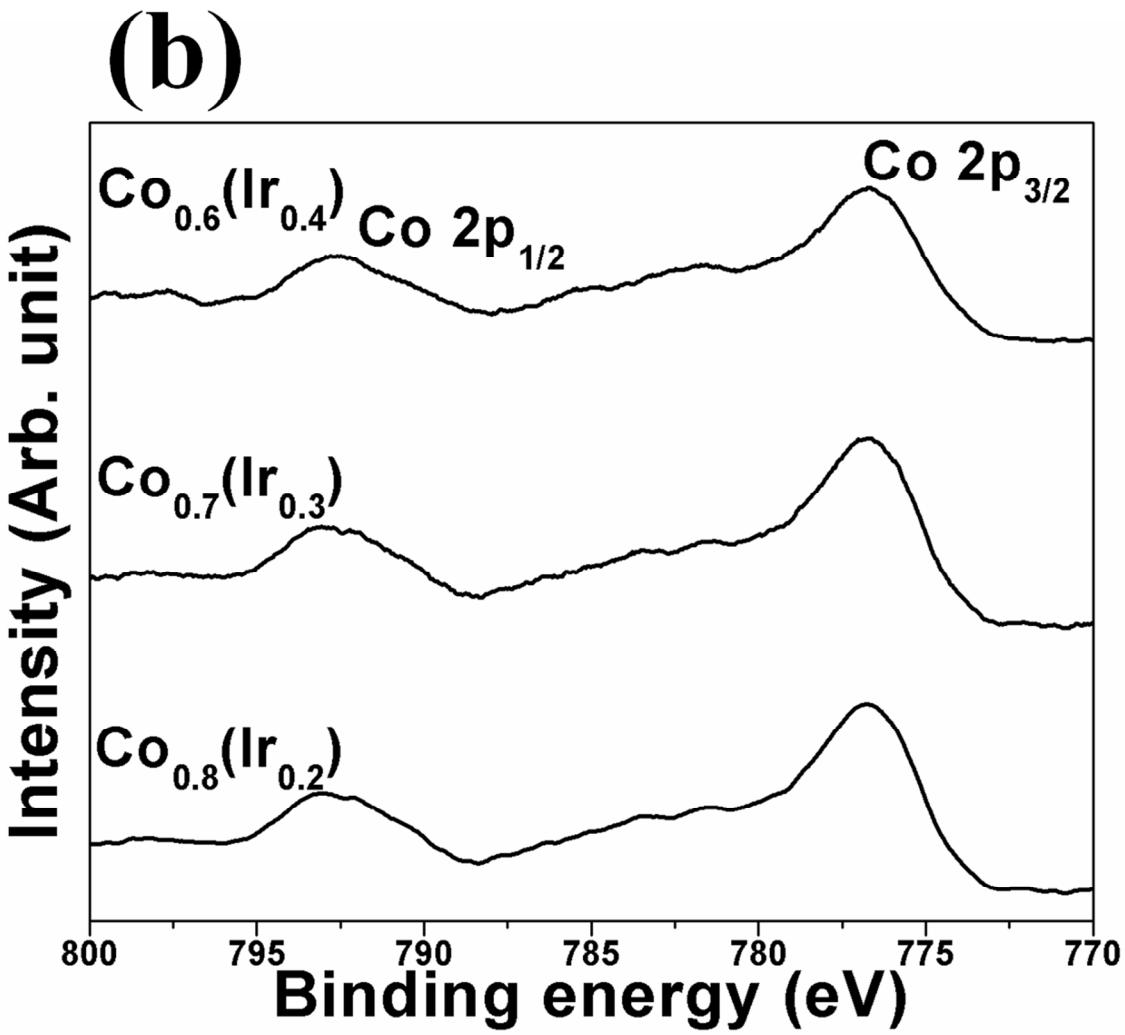

Figure 7: The XPS spectra of $Co_{1-x}(Ir_x)$ showing (a) Ir $4f_{5/2}$ and $4f_{7/2}$ doublet and (b) Co $2p_{1/2}$ and $2p_{3/2}$ doublet

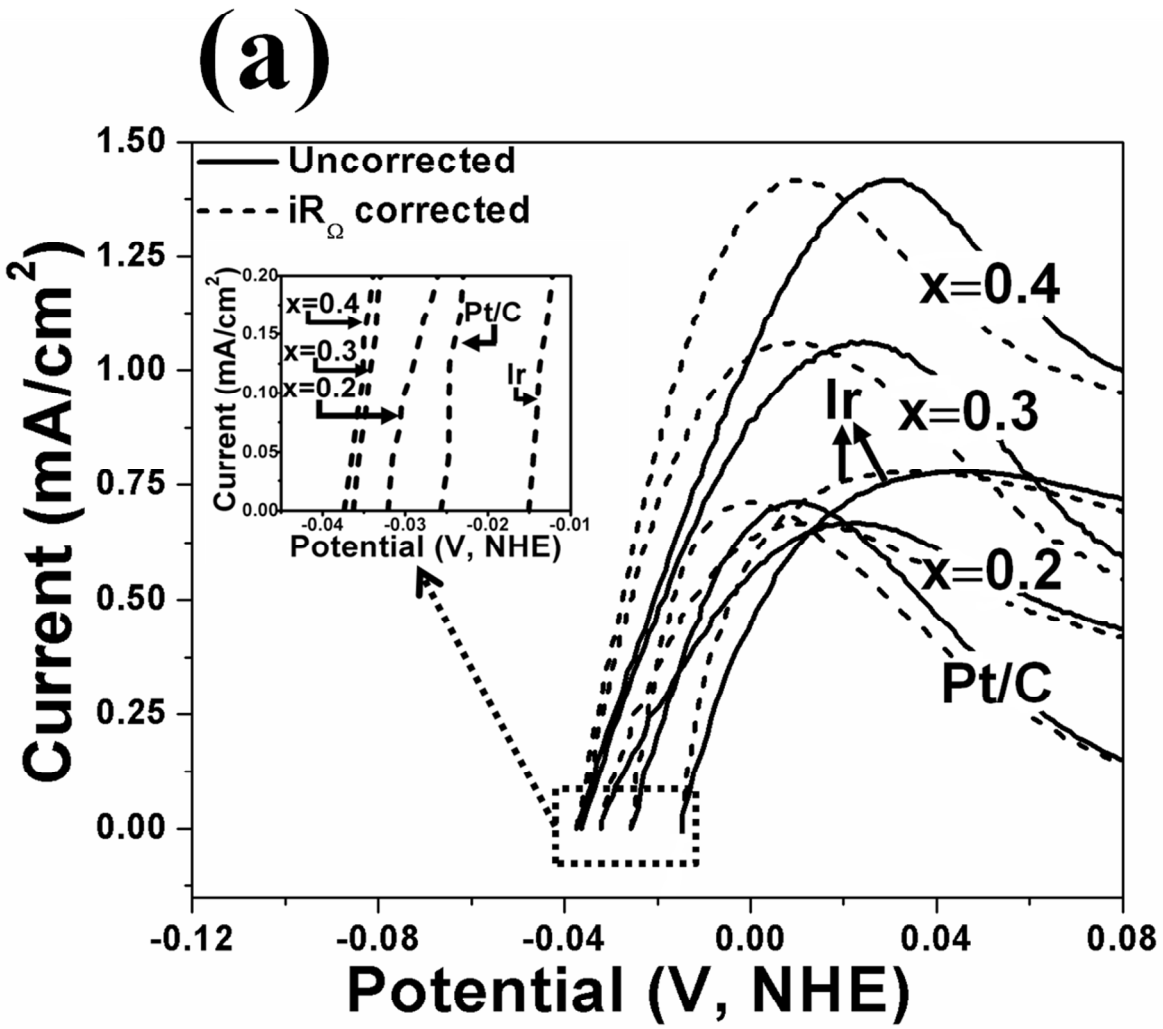

Figure 8: (a) The anodic part of CV curve (**Fig. S3** and **S10**) (between -0.04 V to 0.08 V *vs* NHE) curve for HOR of $Co_{1-x}(Ir_x)$ (x=0.2, 0.3, 0.4, 1) and Pt/C with magnified image between -0.04 V to -0.01 V (*vs* NHE) in inset, measured in H_2 saturated 0.5 M H_2SO_4 at 40^0C at scan rate of 10 mV/sec, before and after iR_Ω correction, (b) Variation of onset potential and current (at 0 V *vs* NHE) with iridium content

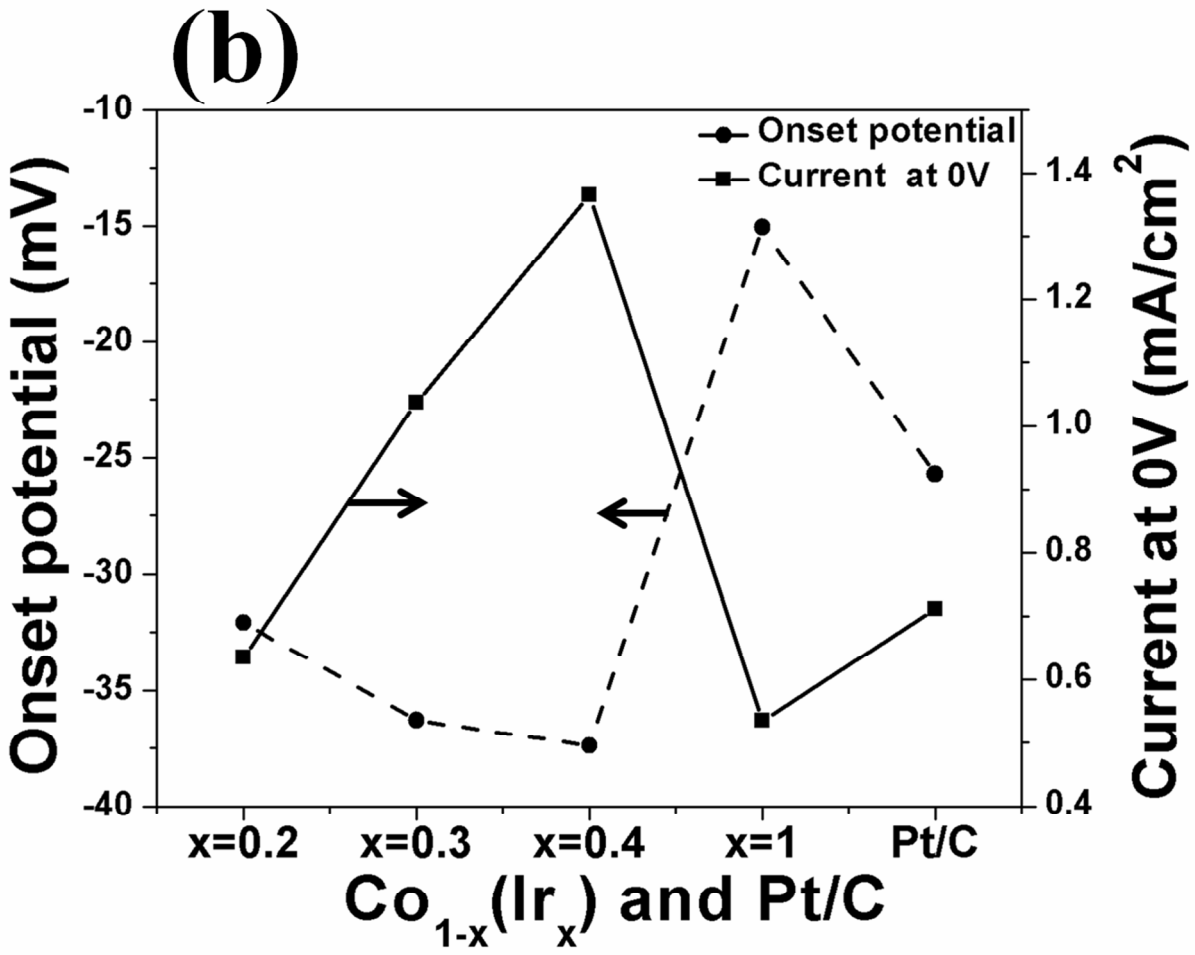

Figure 8: (a) The anodic part of CV curve (**Fig. S3** and **S10**) (between -0.04 V to 0.08 V *vs* NHE) curve for HOR of $Co_{1-x}(Ir_x)$ (x=0.2, 0.3, 0.4, 1) and Pt/C with magnified image between -0.04 V to -0.01 V (*vs* NHE) in inset, measured in H_2 saturated 0.5 M H_2SO_4 at 40^0C at scan rate of 10 mV/sec, before and after iR_Ω correction, (b) Variation of onset potential and current (at 0 V *vs* NHE) with iridium content

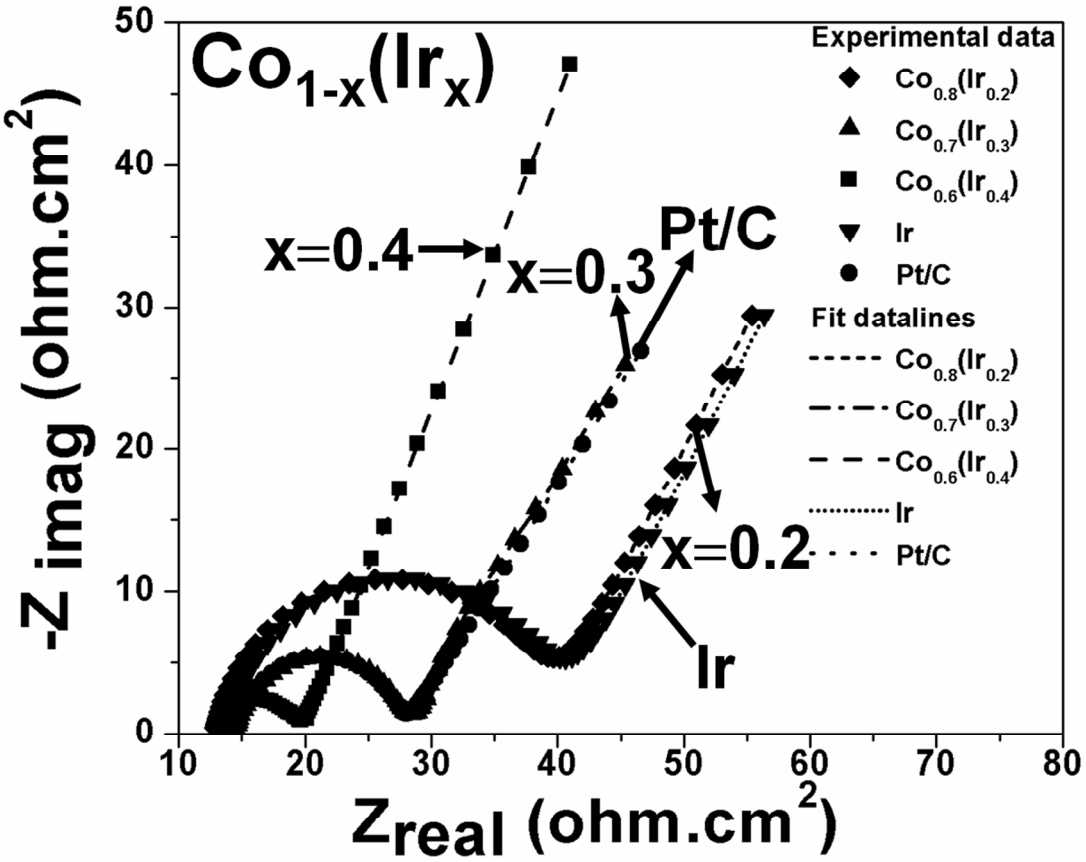

Figure 9: EIS spectra of $Co_{1-x}(Ir_x)$ (x=0.2, 0.3, 0.4, 1) and Pt/C obtained at ~0.016 V (*vs* NHE) in H_2 saturated 0.5 M H_2SO_4 solution at 40^0C in the frequency range of 100 mHz to 100 kHz

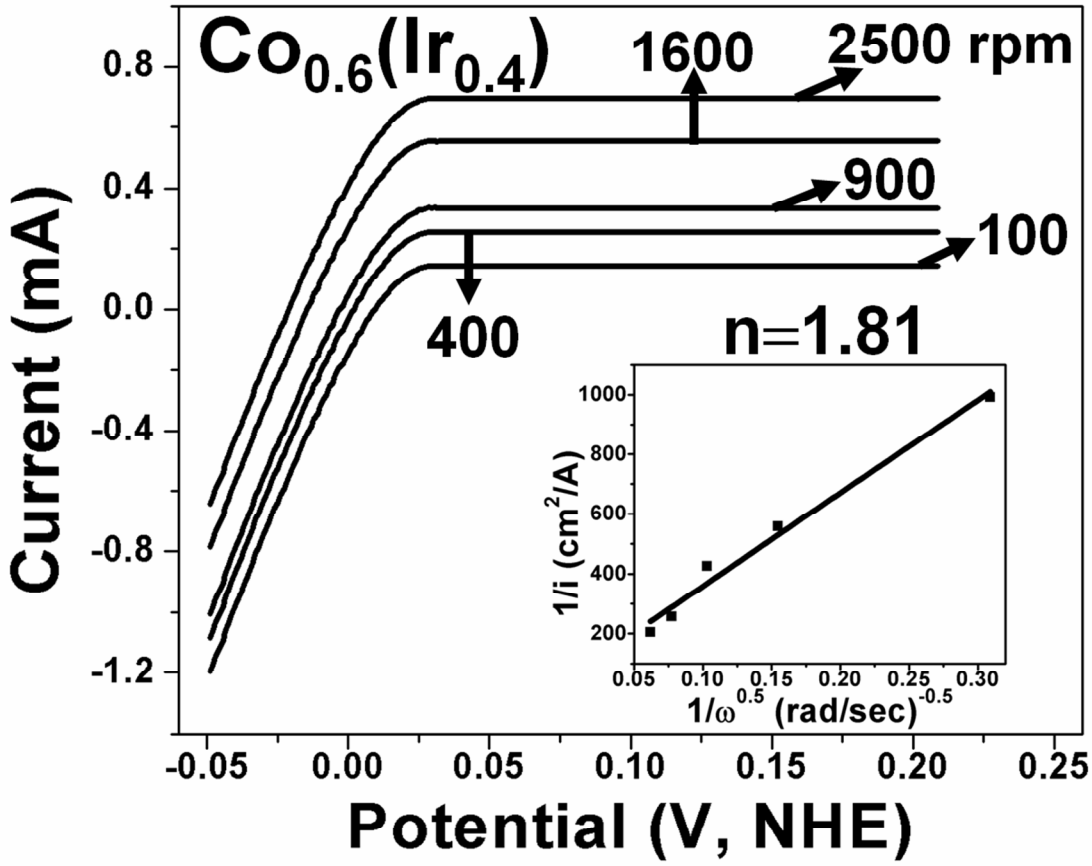

Figure 10: The polarization curve for HOR of $Co_{0.6}(Ir_{0.4})$ obtained on rotating disk electrode (RDE), measured in H_2 saturated 0.5 M H_2SO_4 solution at 40^0C with a scan rate of 10 mV/sec. The Koutechy-Levich plot of $Co_{0.6}(Ir_{0.4})$ is shown in the inset of the polarization curve.

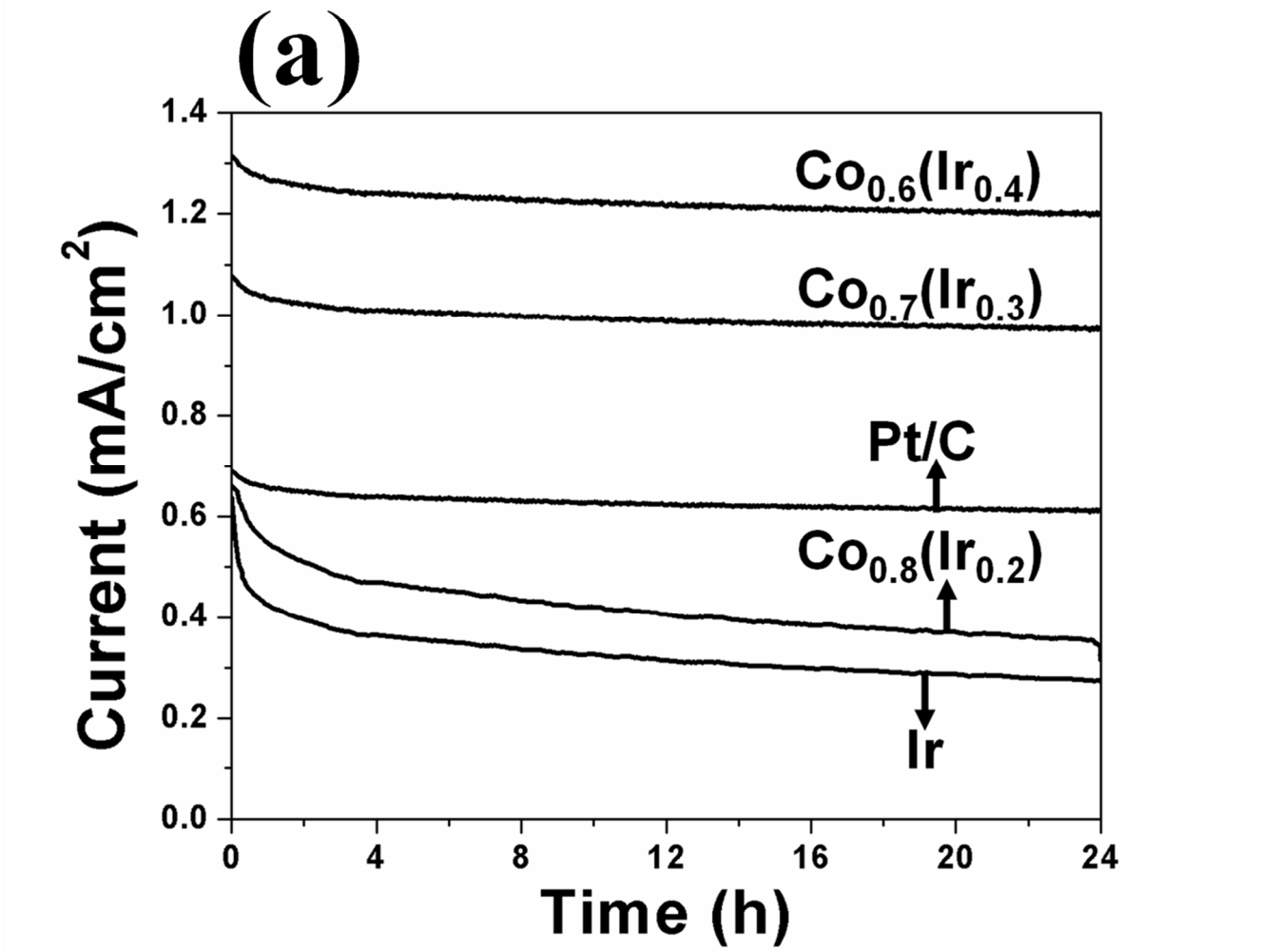

Figure 11: (a) The variation of current *vs* time in the chronoamperometry test of $Co_{1-x}(Ir_x)$ (x=0.2, 0.3, 0.4, 1) and Pt/C, performed in H_2 saturated 0.5 M H_2SO_4 solution under a constant potential of ~0.016 V (*vs* NHE) at 40^0C for 24 h, (b) The cyclic voltammetry (CV) curve for HOR of $Co_{1-x}(Ir_x)$ (x=0.2, 0.3, 0.4), measured in H_2 saturated 0.5 M H_2SO_4 at 40^0C at scan rate of 10 mV/sec, obtained after 24 h chronoamperometry test, (c) The cyclic voltammetry (CV) curve for HOR of Ir NPs and Pt/C, measured in H_2 saturated 0.5 M H_2SO_4 at 40^0C at scan rate of 10 mV/sec, obtained after 24 h chronoamperometry test

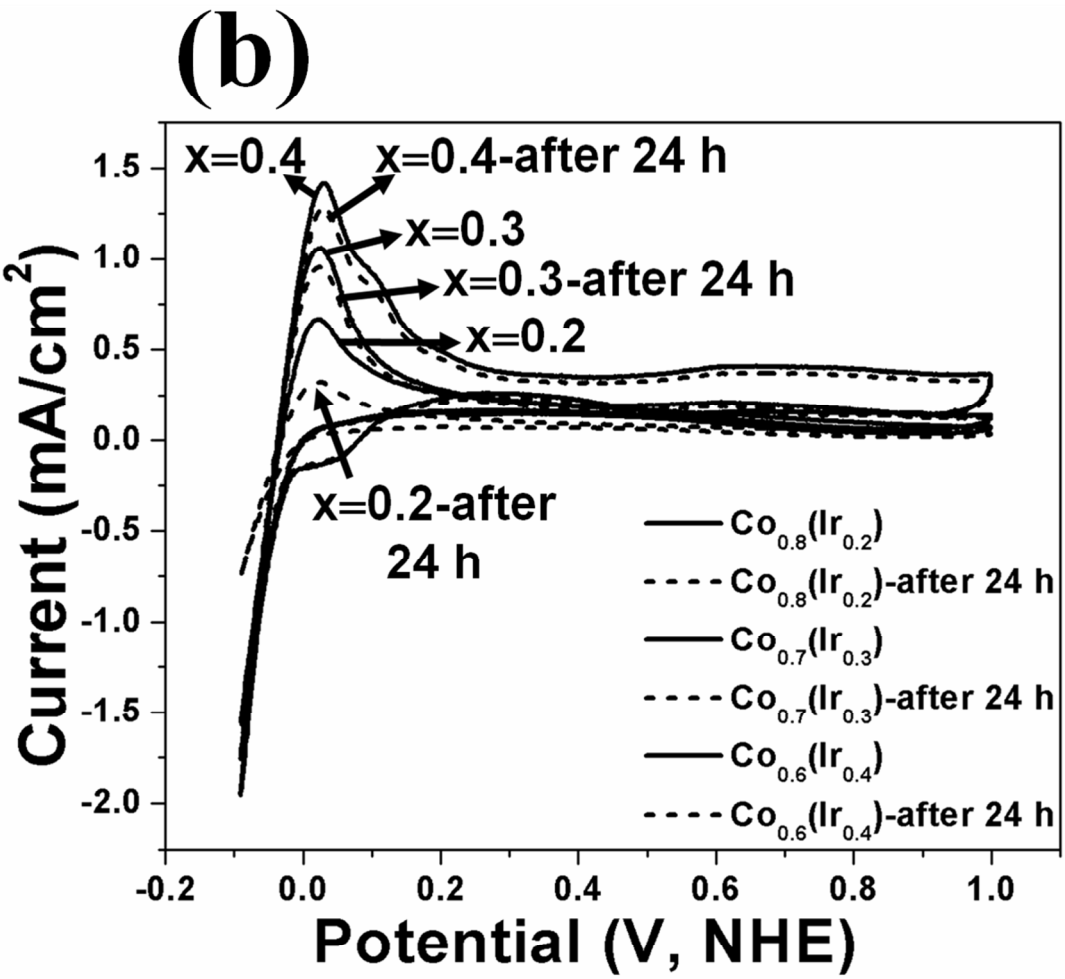

Figure 11: (a) The variation of current *vs* time in the chronoamperometry test of $Co_{1-x}(Ir_x)$ (x=0.2, 0.3, 0.4, 1) and Pt/C, performed in H_2 saturated 0.5 M H_2SO_4 solution under a constant potential of ~0.016 V (*vs* NHE) at 40^0C for 24 h, (b) The cyclic voltammetry (CV) curve for HOR of $Co_{1-x}(Ir_x)$ (x=0.2, 0.3, 0.4), measured in H_2 saturated 0.5 M H_2SO_4 at 40^0C at scan rate of 10 mV/sec, obtained after 24 h chronoamperometry test, (c) The cyclic voltammetry (CV) curve for HOR of Ir NPs and Pt/C, measured in H_2 saturated 0.5 M H_2SO_4 at 40^0C at scan rate of 10 mV/sec, obtained after 24 h chronoamperometry test

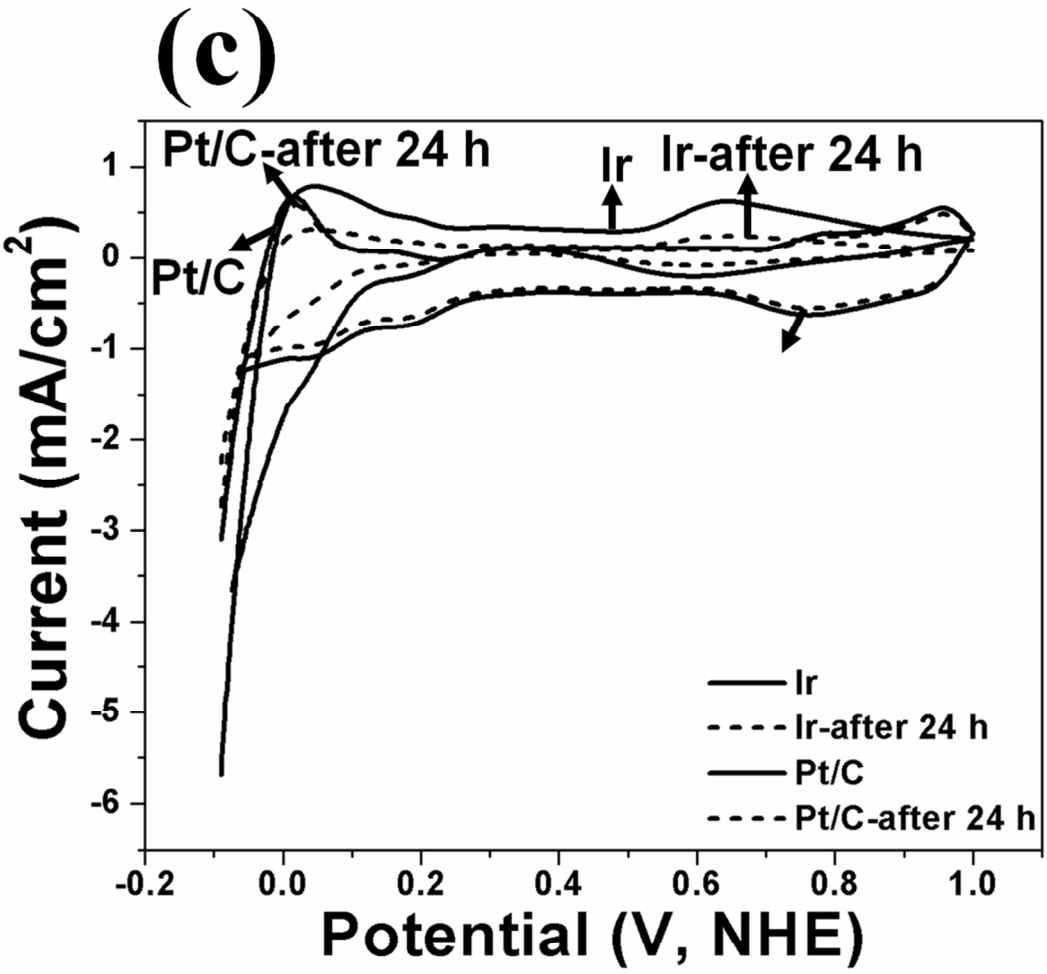

Figure 11: (a) The variation of current *vs* time in the chronoamperometry test of $Co_{1-x}(Ir_x)$ (x=0.2, 0.3, 0.4, 1) and Pt/C, performed in H_2 saturated 0.5 M H_2SO_4 solution under a constant potential of ~0.016 V (*vs* NHE) at 40^0C for 24 h, (b) The cyclic voltammetry (CV) curve for HOR of $Co_{1-x}(Ir_x)$ (x=0.2, 0.3, 0.4), measured in H_2 saturated 0.5 M H_2SO_4 at 40^0C at scan rate of 10 mV/sec, obtained after 24 h chronoamperometry test, (c) The cyclic voltammetry (CV) curve for HOR of Ir NPs and Pt/C, measured in H_2 saturated 0.5 M H_2SO_4 at 40^0C at scan rate of 10 mV/sec, obtained after 24 h chronoamperometry test

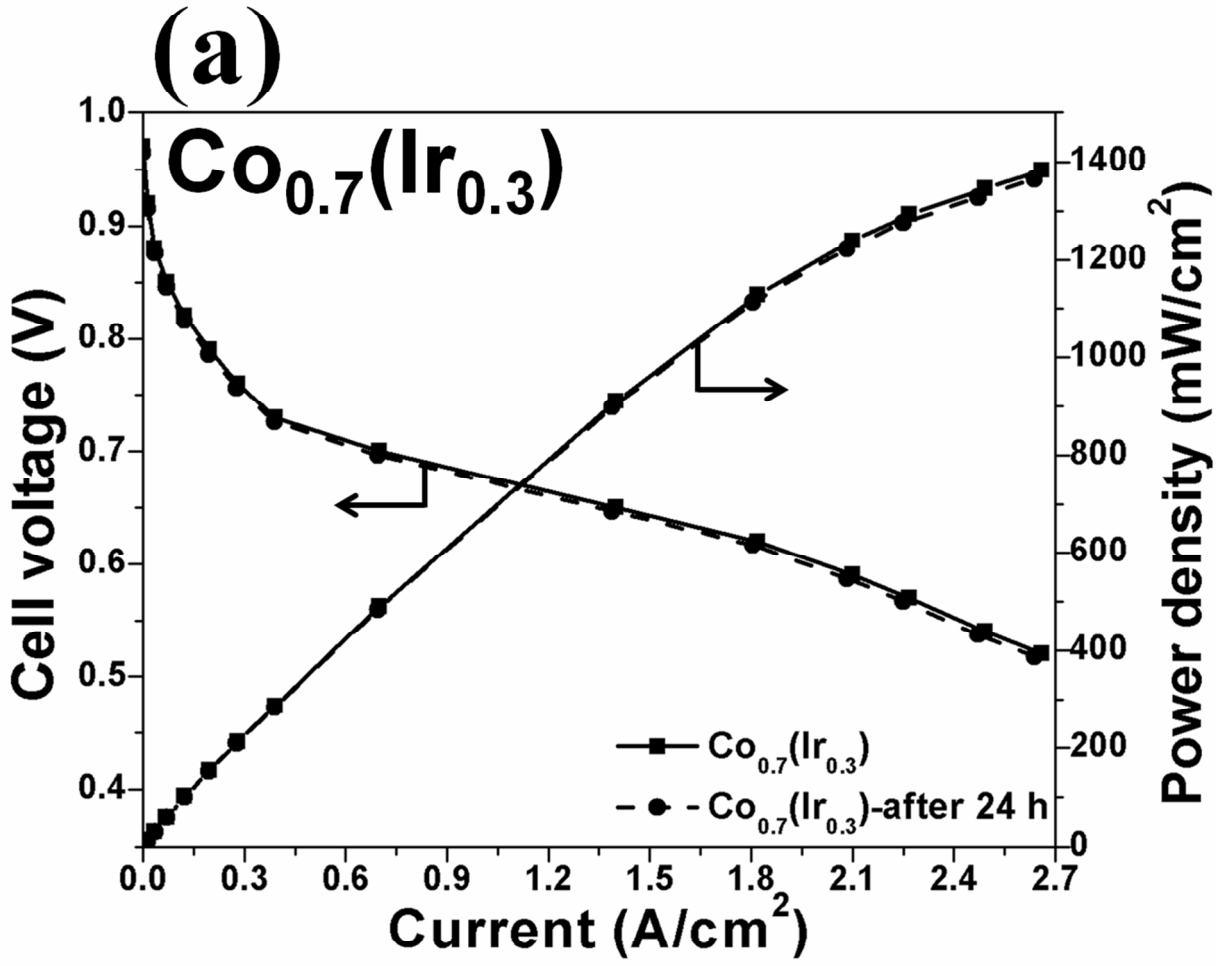

Figure 12: Performance of single PEMFC with (a) $Co_{1-x}(Ir_x)$ (x=0.3) (total loading=0.2 mg/cm^2), (b) $Co_{1-x}(Ir_x)$ (x=0.4) (total loading=0.2 mg/cm^2) and (c) Pt/C (0.2 mg of Pt/cm^2) as anode electro-catalyst and Pt/C (0.3 mg of Pt/cm^2) as cathode electro-catalyst at 80^{0}C and 0.1 MPa with UHP-H_2 (200 ml/min) and UHP-O_2 (300 ml/min) as reactant gases

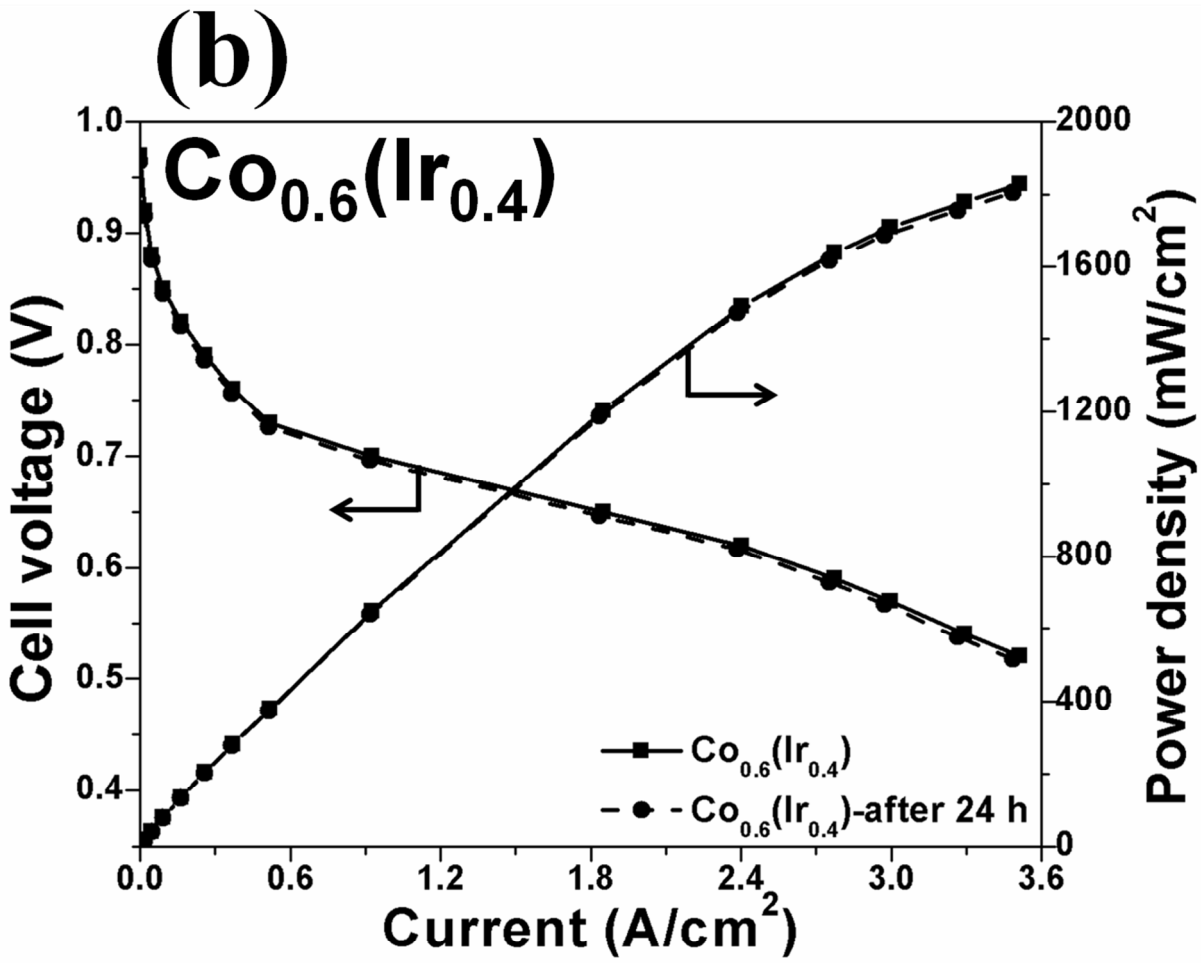

Figure 12: Performance of single PEMFC with (a) $Co_{1-x}(Ir_x)$ (x=0.3) (total loading=0.2 mg/cm^2), (b) $Co_{1-x}(Ir_x)$ (x=0.4) (total loading=0.2 mg/cm^2) and (c) Pt/C (0.2 mg of Pt/cm^2) as anode electro-catalyst and Pt/C (0.3 mg of Pt/cm^2) as cathode electro-catalyst at 80^0C and 0.1 MPa with UHP-H_2 (200 ml/min) and UHP-O_2 (300 ml/min) as reactant gases

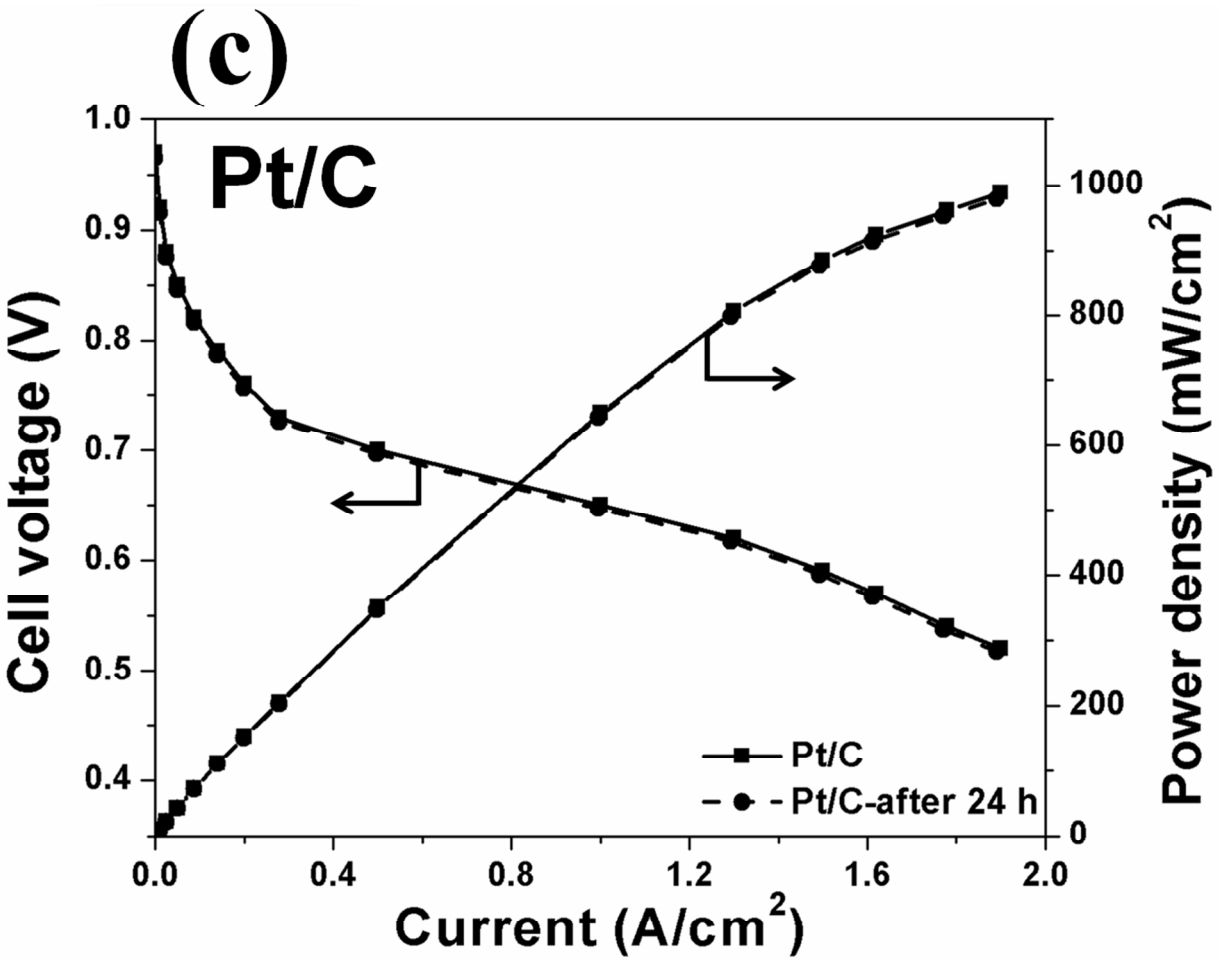

Figure 12: Performance of single PEMFC with (a) $Co_{1-x}(Ir_x)$ (x=0.3) (total loading=0.2 mg/cm^2), (b) $Co_{1-x}(Ir_x)$ (x=0.4) (total loading=0.2 mg/cm^2) and (c) Pt/C (0.2 mg of Pt/cm^2) as anode electro-catalyst and Pt/C (0.3 mg of Pt/cm^2) as cathode electro-catalyst at 80^0C and 0.1 MPa with UHP-H_2 (200 ml/min) and UHP-O_2 (300 ml/min) as reactant gases

1199

Table of contents entry

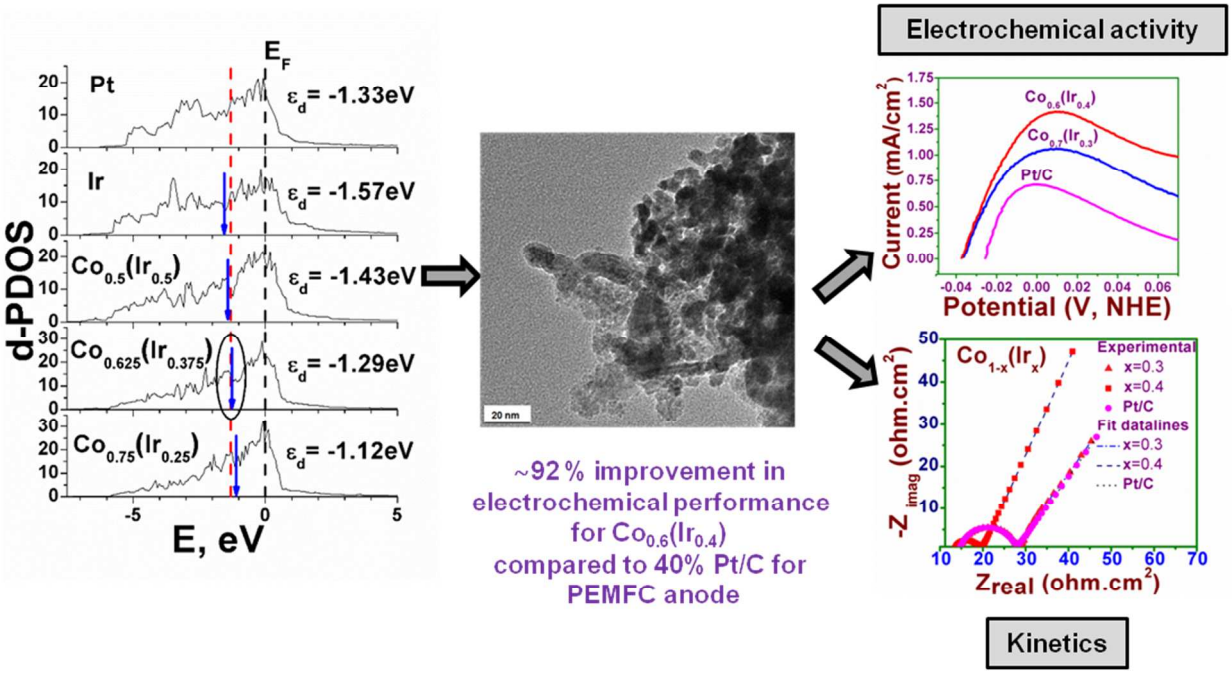

1200